Can mesoscale eddy kinetic energy sources and sinks be inferred from sea surface height in the Agulhas Current ?

Pauline Tedesco[1], Jonathan Gula[2], Pierrick Penven[3], Claire Menesguen[4], Quentin Jamet[5], and Clément Vic[6]

[1]Imperial College London
[2]Université de Bretagne Occidentale
[3]LMI ICEMASA IRD
[4]Ifremer - Laboratoire d'Océanographie Physique et Spatiale
[5]Institut des Géosciences de l'Environnement
[6]Ifremer

November 22, 2022

Abstract

Western boundaries (WB) have been suggested to be hotspots of mesoscale eddy decay, using an eddy kinetic energy (EKE) flux divergence based on sea surface height (η). The η-based diagnostic requires approximations, including the use of geostrophic velocities. Here, we assess to what extent mesoscale EKE flux divergence can be inferred from η using a numerical simulation of the Agulhas Current. The EKE flux divergence is composed of two terms: the eddy-pressure work (linear component) and the advection of EKE (nonlinear component). Both are mainly positive in the WB region (net EKE sources). However, it is not reliably accounted by both η-based diagnostics. The η-based eddy-pressure work has a net contribution in the WB region of the opposite sign than the true one. Ageostrophic eddy-pressure work dominates the geostrophic one (corresponding to a β-contribution). It is explained by mesoscale eddies's scale to fall below the scale of ζ/β (ζ: root mean square of normalized relative vorticity for mesoscale eddies; β: latitudinal variations of Coriolis parameter). The advection done by geostrophic EKE flux dominates the EKE flux divergence in the WB region. It results in the EKE flux divergence to be qualitatively estimable using η (up to 54 % of the net EKE source). Our results in the Agulhas Current show a mesoscale eddy dynamics in contrast with the decay's paradigm at western boundaries. Further analysis in other western boundaries are required to complete our understanding of mesoscale eddies dynamics.

Can mesoscale eddy kinetic energy sources and sinks be inferred from sea surface height in the Agulhas Current ?

P. Tedesco[1,2], J. Gula[1,3], P. Penven[1], C. Ménesguen[1], Q. Jamet[4], C. Vic[1]

[1]Univ. Brest, CNRS, IRD, Ifremer, Laboratoire d'Océanographie Physique et Spatiale (LOPS), IUEM, 29280, Brest, France.
[2]Imperial College of London, London, UK.
[3]Institut Universitaire de France (IUF), Paris, France.
[4]Institut des Géosciences de l'Environnement (IGE), Grenoble, France.

Key Points:

- The mesoscale EKE flux divergence is overall positive in the Agulhas Current region, highlighting a net mesoscale EKE source
- Coupled geostrophic-ageostrophic EKE flux significantly contributing to the net EKE source cannot be inferred using sea surface height
- Advection done by geostrophic EKE flux dominates the net EKE source and can be inferred using sea surface height

Corresponding author: Pauline Tedesco, p.tedesco@imperial.ac.uk

Abstract

Western boundaries (WB) have been suggested to be hotspots of mesoscale eddy decay, using an eddy kinetic energy (EKE) flux divergence based on sea surface height (η). The η-based diagnostic requires approximations, including the use of geostrophic velocities. Here, we assess to what extent mesoscale EKE flux divergence can be inferred from η using a numerical simulation of the Agulhas Current. The EKE flux divergence is composed of two terms: the eddy-pressure work (linear component) and the advection of EKE (nonlinear component). Both are mainly positive in the WB region (net EKE sources). However, it is not reliably accounted by η-based diagnostics. The η-based eddy-pressure work has a net contribution in the WB region of the opposite sign than the true one. Ageostrophic eddy-pressure work dominates the geostrophic one (corresponding to a β-contribution). It is explained by mesoscale eddies's scale to fall below the scale of $\frac{\zeta'_{RMS}}{\beta}$ (ζ'_{RMS}: normalized relative vorticity for mesoscale eddies; β: latitudinal variations of Coriolis parameter). The advection of EKE done by geostrophic EKE flux dominates the EKE flux divergence in the WB region. It results in the EKE flux divergence to be qualitatively estimable using η (up to 54% of the net EKE source). Our results in the Agulhas Current show a mesoscale eddy dynamics in contrast with the decay's paradigm at western boundaries. Further analysis in other western boundaries are required to complete our understanding of mesoscale eddies dynamics.

Plain Language Summary

Large-scale eddies are a key component of the ocean energy budget. Although their generation is largely documented, how their energy is dissipated remains uncertain. A closure to their lifecycle — decay at western boundaries of oceanic basins — has been suggested using satellite observations of the sea surface. However, using sea surface observations requires several approximations on the ocean dynamics. Understanding to what extent, the large-scale eddies dynamics can be inferred from sea surface observations is a fundamental issue for study strategies. Here, we investigate the impacts of the approximations, on the net energy sources and sinks of large-scale eddies, using a numerical simulation of the Agulhas Current. We show that the Agulhas Current is a net energy source of large-scale eddies, which can be qualitatively inferred using sea surface observations. The net energy source is mainly explained by turbulent motions and more weakly, but still significantly by wave-like motions. The leading order velocities of turbulent motions can be inferred from sea surface observations. Our results in the Agulhas Current are favorable to the use of sea surface observations, but show a dynamics in contrast with the decay's paradigm at western boundaries.

1 Introduction

Mesoscale eddies represent 90 % of the surface kinetic energy (Wunsch, 2007) and are a key component of the global ocean energy budget (Ferrari & Wunsch, 2009; Müller et al., 2005). They have horizontal scales of the order of the 1^{st} Rossby deformation radius (Rd) or larger (Chelton et al., 2011). At these scales, the velocity field can be decomposed into a leading order geostrophic and a weaker ageostrophic component based on the quasi-geostrophic theory (Gill, 1982). Geostrophy represents the balance of flows dominated by rotation compared to advection (Rossby number : $Ro \ll 1$) and stratification compared to vertical shear (Richardson number : $Ri \gg 1$). At scales comparable to or smaller than Rd, the dynamics departs from geostrophy ($Ro, Ri \sim O(1)$) and ageostrophic effects, such as advection, vertical shear and topographic interactions among others, can play an important role.

The characteristics of mesoscale eddies make them easily trackable by satellite altimetry, which measures sea surface height (η). The low-frequency component of sea-surface height is an indirect measure of the surface geostrophic currents. Satellite altimetry allowed to improve our understanding of the ocean dynamics by evidencing the prevalence of mesoscale eddies at the surface (Ducet et al., 2000). Although mesoscale eddies are ubiquitous across the ocean, they are the most energetic in western boundary currents and in the Antarctic Circumpolar Current (Ducet et al., 2000; Chelton et al., 2007, 2011), making these regions key spots for the global ocean energy budget.

Western boundaries have been suggested to be mesoscale eddy kinetic energy (EKE) sinks (Zhai et al., 2010). This suggestion closes the following paradigm of mesoscale eddy lifecycle: mesoscale eddies originate nearly everywhere in the ocean, propagate westward at about the speed of long baroclinic Rossby waves and decay upon western boundaries, likely due to direct energy routes, down to dissipation, channeled by topography (Gill et al., 1974; Zhai et al., 2010; Chelton et al., 2011; Evans et al., 2020; Z. Yang et al., 2021; Evans et al., 2022). This scenario has been confirmed, using *in situ* measurements and idealized numerical simulations, in regions free of western boundary current (Evans et al., 2020; Z. Yang et al., 2021; Evans et al., 2022). However, in the presence of western boundary currents, studies based on numerical simulations show more complex mesoscale eddy dynamics. Western boundaries are hotspots of mesoscale eddy generation due to instabilities of the western boundary currents (Halo et al., 2014; Kang & Curchitser, 2015; Gula et al., 2015; Y. Yang & Liang, 2016; Yan et al., 2019; Li et al., 2021; Jamet et al., 2021; Tedesco et al., 2022), such that local generation of mesoscale eddies may overcome the local decay of remotely-generated mesoscale eddies.

Sources and sinks of mesoscale EKE can be estimated by computing the EKE flux divergence. A negative (positive) EKE flux divergence shows a net EKE sink (source). The EKE flux divergence corresponds to the rate of the spatial redistribution of EKE. It has two components : the work done by pressure fluctuations (eddy-pressure work; usually interpreted as the linear contribution from the waves) and the nonlinear advection of EKE by the flow (Harrison & Robinson, 1978).

Using an η-based EKE flux divergence, Zhai et al. (2010) estimated a mesoscale EKE sink. Their vertically-integrated EKE flux divergence based on η relies on three approximations:

(i) **Mesoscale eddies are assumed to be geostrophic**. Geostrophy should be a good approximation for mesoscale eddy velocities, as assumed by the quasi-geostrophic turbulence theory (Charney, 1971) and indicated by the Rossby number of mesoscale eddies ($Ro = O(\ll 0.05)$) inferred from satellite altimetry (Chelton et al., 2011).

(ii) **The mesoscale eddy vertical structure is approximated by the 1^{st} baroclinic mode**. η is a measure of the ocean surface dynamics and is usually interpreted as primarily reflecting the 1^{st} baroclinic mode, which has a surface-intensified structure (Wunsch, 1997; Smith & Vallis, 2001). It relates to mesoscale eddies which have surface-intensified vertical structures energized to the bottom, represented by the combination of the barotropic and 1^{st} baroclinic vertical modes (Wunsch, 1997; Smith & Vallis, 2001; Venaille et al., 2011; Tedesco et al., 2022).

(iii) **Mesoscale eddies interactions with topography are neglected**. This might be justified by assuming that mesoscale EKE flux have spatial variations larger than that of topography (Zhai et al., 2010).

Several studies, based on numerical simulations and using no approximations, denote a EKE flux divergence in contrast with the η-based one (Harrison & Robinson, 1978; Chen et al., 2014; Capó et al., 2019). The eddy-pressure work is mainly negative and of leading order in most regions (western boundary currents, Antarctic Circumpolar Current, Subtropical gyre and Interior Ocean). The advection of EKE is positive in most western boundary currents and in the Western Mediterranean Sea, but it is the leading order contribution only in the latter region. It indicates that the eddy-pressure work and advection of EKE have contrasted contributions, resulting in an EKE flux divergence varying between western boundaries. A recent study has shown that both mesoscale eddy-pressure work and advection of EKE are positive in the Agulhas Current region (Tedesco et al., 2022). This region is a net mesoscale EKE source, in contrast with the paradigm of net mesoscale EKE sinks at western boundaries.

The differences between the non-approximated and the η-based EKE flux divergence question the approximations used to derive the η-based diagnostic. Due to the leading order geostrophic component of mesoscale eddy, satellite altimetry is a reference database for evaluating the surface mesoscale EKE reservoir. However, the question of using altimetry data to assess the sources and sinks of mesoscale EKE remains a separate issue. The quasi-geostrophic theory states that ageostrophic motions significantly contribute to the processes sustaining the mesoscale EKE reservoir (Müller et al., 2005; Ferrari & Wunsch, 2009). While the significance of ageostrophic motions to energy transfers across scales, and especially from mesoscale eddies toward smaller scales, is asserted, its contributions to the EKE flux divergence remains an open question to our knowledge.

Surface geostrophic velocities derived from satellite altimetry data are usually interpreted as primarily reflecting the 1^{st} baroclinic mode (Wunsch, 2007; Smith & Vallis, 2001). However, this questions the interpretation of the η-based EKE flux divergence as the one of the mesoscale reservoir, which is formally represented by the barotropic and 1^{st} baroclinic modes (Wunsch, 1997; Smith & Vallis, 2001; Venaille et al., 2011). This question is supported by a study showing that the increasing resolution of eddies results in an increasing EKE fraction into the baroclinic mode (Yankovsky et al., 2022). It is also supported by a study showing that the mesoscale EKE reservoir is equipartitioned between both modes, or even locally dominated by the barotropic mode, in the western boundary region of the Agulhas Current (Tedesco et al., 2022).

Topographic interactions are documented to be key processes of mesoscale eddy dynamics at western boundaries. Topography controls instability processes (Lutjeharms, 2006; Gula et al., 2015) and channels energy transfers between mesoscale eddies, eddies of smaller scale, waves and mean currents (Adcock & Marshall, 2000; Nikurashin & Ferrari, 2010; Evans et al., 2020; Perfect et al., 2020; Tedesco et al., 2022). The contribution of topographic interactions to mesoscale EKE flux divergence remains to be determined.

Assessing to what extent altimetry data allows to infer mesoscale EKE flux divergence is an important step toward improving our understanding of the global ocean dynamics. It depends on the impact of the three aforementioned approximations – (i) geostrophy *vs.* ageostrophy, (ii) 1^{st} baroclinic *vs.* barotropic modes and (iii) importance of topographic interactions – in regions of western boundary. We aim to assess the impact of approximations (i), (ii), and (iii) on the mesoscale EKE flux divergence using a numerical simulation of the Agulhas Current. The latter one is the western boundary current of the South Indian Ocean (Lutjeharms, 2006) and a sub-region of the largest mesoscale EKE sink, found at the western boundary of the South Indian Ocean, by Zhai et al. (2010).

Our study is organized around the following questions : Do the η-based components of the EKE flux divergence (eddy-pressure work and advection of EKE) provide reliable estimates of the true ones ? If not, which approximations are responsible for differences ? What are the implications for inferring the EKE flux divergence using η field ? The true and η-based expressions of EKE flux divergence components (eddy-pressure work and advection of EKE) are defined and interpreted in section 2. The η-based paradigm of mesoscale EKE sink at western boundaries (Zhai et al., 2010) is evaluated using observations and a numerical simulation in section 3. The validity of the η-based components are evaluated and the main contributions of the true components are characterized, respectively in section 4 and 5. The results of sections 4 and 5 are sum up in section 6 to draw a conclusion on the use of satellite altimetry data to infer the EKE flux divergence. The results are then discussed in a larger context of observation-based EKE budgets and of mesoscale eddy dynamics in section 7.

2 Theory

We present in the following the modal EKE flux divergence. We first present the theoretical framework of vertical modes. We then define the true expression of the EKE flux divergence, constituted of the modal eddy-pressure work (EPW) and the advection of EKE ($AEKE$), based on Tedesco et al. (2022). We finally detail the approximations that are required to derive their η-based expressions.

2.1 Vertical modes

A convenient approach to describe the vertical structure of mesoscale motions is the modal decomposition using traditional vertical modes (Gill, 1982). The vertical structure of the mesoscale EKE reservoir corresponds to the combination of the barotropic and 1^{st} baroclinic modes (Wunsch, 1997; Smith & Vallis, 2001; Venaille et al., 2011; Tedesco et al., 2022), which represents surface-intensified vertical structures energized to the bottom.

The vertical modes ϕ_n for the horizontal velocity ($\mathbf{u}$) and the dynamical pressure (p) are the eigenfunctions solution of the Sturm-Liouville problem (Eq. 1), using linearized free-surface ($|\frac{\partial}{\partial z}\phi_n|_{z=\eta} = |\frac{-\overline{N^2}}{g}\phi_n|_{z=\eta}$) and flat-bottom boundary conditions ($|\frac{\partial}{\partial z}\phi_n|_{z=-H} = 0$) :

$$\frac{\partial}{\partial z}\left(\frac{1}{N^2}\frac{\partial}{\partial z}\phi_n\right) + \frac{1}{c_n^2}\phi_n = 0 \tag{1}$$

with N^2 the time-averaged buoyancy frequency, g the acceleration of gravity and $c_n^2 = \frac{1}{n\pi}\int_{-H}^{\eta} N(\mathbf{x}, z)\ dz$ the eigenvalues of the vertical modes.

The vertical modes are related to horizontal scales via c_n^2, which are good approximations of the Rossby baroclinic deformation radii : $Rd_{n\geq 1} = \frac{c_n}{|f|}$ (Chelton et al., 1998), with f the Coriolis parameter. The modal base ϕ_n satisfies the orthogonality condition :

$$\int_{-H}^{\eta} \phi_m \phi_n\ dz = \delta_{mn} h \tag{2}$$

with δ_{mn} the usual Kronecker symbol and $h = \eta + H$ the water column depth.

The dynamical variables are projected onto n vertical modes as follows :

$$[\mathbf{u}_n(\mathbf{x}, t), \frac{1}{\rho_0}p_n(\mathbf{x}, t)] = \frac{1}{h}\int_{-H}^{\eta} [\mathbf{u}(\mathbf{x}, z, t), \frac{1}{\rho_0}p(\mathbf{x}, z, t)]\phi_n(\mathbf{x}, z)\ dz \tag{3}$$

with $\mathbf{u}_n$ and p_n the modal amplitudes of the horizontal velocity ($\mathbf{u}$) and dynamical pressure (p) and ρ_0 the reference density value.

2.2 True expression of the modal *EKE* flux divergence

The modal EKE flux divergence is a contribution of the modal EKE budget. The modal EKE budget corresponds to the classic EKE budget (Harrison & Robinson, 1978; Gula et al., 2016) derived in the framework of the vertical modes. Tedesco et al. (2022) derived a comprehensive modal EKE budget in the context of the mesoscale variability, inspired from the budget derived in the context of internal tides (Kelly, 2016). The modal EKE budget reads as follows :

$$\underbrace{\mathbf{u'_n} \cdot (\rho_0 h \frac{\partial}{\partial_t} \mathbf{u'_n})}_{Time\ rate} + \underbrace{\underbrace{\nabla_H \cdot \int_{-H}^{\eta} \mathbf{u'}_n p'_n \phi_n^2 \, dz}_{Eddy-pressure\ work\ (EPW)} + \underbrace{\frac{\rho_0}{2} \nabla_H . \int_{-H}^{\eta} \mathbf{u}_n \phi_n ||\mathbf{u'}_n \phi_n||^2 \, dz}_{Advection\ of\ EKE\ (AEKE)}}_{Modal\ EKE\ flux\ divergence\ (EPW+AEKE)} = \sum \left(\underbrace{S_n}_{EKE\ sources} + \underbrace{D_n}_{EKE\ sinks} \right) \tag{4}$$

with the prime denoting fluctuations relative to the 1995-2004 time average. Terms are averaged over this period. The dynamical pressure ($p(\mathbf{x}, z, t)$) is derived from the *in situ* density ($\rho(\mathbf{x}, z, t)$) from which the background density profile ($\widetilde{\rho}(z)$ defined as the spatial and time average of the *in situ* density) has been substracted.

The modal EKE flux divergence corresponds to the rate of the spatial redistribution of modal EKE done by pressure fluctuations (EPW) and by advection ($AEKE$). The EPW is usually interpreted as the linear wave contribution, and $AEKE$ as the advection of EKE by the total flow (Harrison & Robinson, 1978). In the context of linear theories of internal waves (Kelly et al., 2010, 2012; Kelly, 2016) and of Rossby waves (Masuda, 1978), EPW is the only contribution to the modal EKE flux divergence. For interior-ocean dynamics it represents the main contribution (Harrison & Robinson, 1978). In regions of high variability, $AEKE$ can significantly contribute to the EKE flux divergence and can be equivalent to EPW (Harrison & Robinson, 1978; Capó et al., 2019; Tedesco et al., 2022).

The mesoscale eddy dynamics modeled by our numerical simulation is in equilibrium for the period considered in our study (1995-2004). The time rate smallness has indeed been evaluated by Tedesco et al. (2022) for the period 1995-1999, which is shorter than the period 1995-2004 used here. The modal EKE flux divergence therefore accounts for the left hand side of the modal EKE budget (Eq. 4). It equals the sum of all local EKE sources (S_n) and sinks (D_n). It can therefore be interpreted as the redistribution rate of the net EKE sources and sinks. A negative (positive) EKE flux divergence indicates that the ingoing EKE flux are larger (lower) than the outgoing ones, resulting in a net EKE sink (source), whose content has been imported (exported).

In the present study, we focus on the EKE flux divergence of the mesoscale reservoir, that we define as the sum of the barotropic ($n = 0$) and 1^{st} baroclinic ($n = 1$) components ($EPW_{n=0-1}$ and $AEKE_{n=0-1}$ that are referred to EPW and $AEKE$ in the following in order to simplify the notations).

2.3 η-based expressions of the modal *EKE* flux divergence

We define the different η-based expressions of EPW, gradually accounting for approximations (i), (ii) and (iii) used in Zhai et al. (2010). We also define an η-based expression of $AEKE$ accounting for approximation (i). The main terms discussed in this study are listed in Table 1.

2.3.1 Approximation (i) ($EPW_{(i)}$ and $AEKE_{(i)}$)

EPW and $AEKE$ (Eq. 4) can be written as the sum of three contributions, as follows :

$$EPW = \underbrace{\int_{-H}^{\eta} p'_n\phi_n \nabla_H \cdot (\mathbf{u}'_n\phi_n)\ dz}_{\mathbf{A}} + \underbrace{\int_{-H}^{\eta} (\mathbf{u}'_n\phi_n)\cdot\nabla_H(p'_n\phi_n)\ dz}_{\mathbf{B}} + \underbrace{\nabla_H\eta\cdot|\mathbf{u}'_n p'_n\phi_n^2|_{z=\eta} + \nabla_H H\cdot|\mathbf{u}'_n p'_n\phi_n^2|_{z=-H}}_{\mathbf{C}} \tag{5}$$

$$AEKE = \underbrace{\frac{\rho_0}{2}\int_{-H}^{\eta} ||\mathbf{u}'_n\phi_n||^2\nabla_H\cdot(\mathbf{u}_n\phi_n)\ dz}_{\mathbf{A}} + \underbrace{\frac{\rho_0}{2}\int_{-H}^{\eta}(\mathbf{u}_n\phi_n)\cdot\nabla_H||\mathbf{u}'_n\phi_n||^2\ dz}_{\mathbf{B}} + \underbrace{\frac{\rho_0}{2}\nabla_H\eta\cdot|\mathbf{u}_n\phi_n||\mathbf{u}'_n\phi_n||^2|_{z=\eta} + \frac{\rho_0}{2}\nabla_H H\cdot|\mathbf{u}_n\phi_n||\mathbf{u}'_n\phi_n||^2|_{z=-H}}_{\mathbf{C}} \tag{6}$$

Terms **C** represent the interactions of EKE flux with topography ($-H$) and sea surface height (η) gradients. It can be further simplified to interactions with topographic gradients, because : $||\nabla_H\eta|| = O(10^{-4})||\nabla_H H||$ in the Agulhas Current region.

EPW (Eq. 5) and $AEKE$ (Eq. 6) can be written as $EPW_{(i)}$ (Eq. 7) and $AEKE_{(i)}$ (Eq. 8) when using the approximation of (i) modal geostrophic velocities ($\mathbf{u}'_{g,n}\phi_n$). The velocities are expressed using modulated η fields, which account for the fraction of the different vertical modes ($\mathbf{u}_{g,n}\phi_n = \mathbf{k}\wedge\frac{g}{f}\nabla_H\left(\frac{\phi_n}{|\phi_n|_{z=0}}\lambda_n\eta\right)$ with $\lambda_n = \frac{\eta_n}{\eta}$ and $\mathbf{u}'_{g,n}\phi_n = \mathbf{k}\wedge\frac{g}{f}\nabla_H\left(\frac{\phi_n}{|\phi_n|_{z=0}}\alpha_n\eta'\right)$ with $\alpha_n = \frac{\eta'_n}{\eta'}$).

$$EPW_{(i)} = \underbrace{-\frac{\beta\rho_0 g^2}{2f^2}\frac{\partial}{\partial x}\left(\frac{\int_{-H}^{\eta}\phi_n^2\ dz}{|\phi_n^2|_{z=0}}\alpha_n^2\eta'^2\right)}_{\beta-contribution\ (\mathbf{A1})} + \underbrace{\frac{\beta\rho_0 g^2}{2f^2}\frac{\partial H}{\partial x}\frac{|\phi_n^2|_{z=-H}}{|\phi_n^2|_{z=0}}\alpha_n^2\eta'^2}_{\beta-contribution\ to\ topographic\ interactions\ (\mathbf{A2})} + \underbrace{\frac{\rho_0 g^2}{2f}\nabla_H H\cdot|\mathbf{k}\wedge\nabla_H\left(\frac{\phi_n^2}{|\phi_n^2|_{z=0}}\right)\alpha_n^2\eta'^2|_{z=-H}}_{EKE\ flux-topographic\ interactions\ (\mathbf{C})} \tag{7}$$

With approximation (i), the contribution of horizontal modal pressure gradients (**B** in Eq. 5) cancels out. $EPW_{(i)}$ is therefore constituted of a β-contribution acting on EKE flux (**A1**) and topographic interactions (**A2**) and of the contribution of EKE flux-topographic interactions (**C**).

$$AEKE_{(i)} = \underbrace{-\frac{\beta\rho_0 g}{2f^2}\int_{-H}^{\eta}||\mathbf{u}'_{g,n}\phi_n||^2\frac{\partial}{\partial x}\left(\frac{\phi_n}{|\phi_n|_{z=0}}\lambda_n\eta\right)\ dz}_{\beta-contribution\ (\mathbf{A})} + \underbrace{\frac{\rho_0}{2}\int_{-H}^{\eta}(\mathbf{u}_{g,n}\phi_n)\cdot\nabla_H||\mathbf{u}'_{g,n}\phi_n||^2\ dz}_{Work\ of\ eddy-total\ flow\ interactions\ (\mathbf{B})} + \underbrace{\frac{\rho_0}{2}\nabla_H H\cdot|\mathbf{u}_{g,n}\phi_n||\mathbf{u}'_{g,n}\phi_n||^2|_{z=-H}}_{EKE\ flux-topographic\ interactions\ (\mathbf{C})} \tag{8}$$

$AEKE_{(i)}$ (Eq. 8) is constituted of a β-contribution (**A**), the work of eddy-total flow interactions (**B**) and of the EKE flux-topographic interactions (**C**).

2.3.2 Approximation (ii) ($EPW_{(i,ii)}$)

$EPW_{(i)}$ (Eq. 7) can be written as $EPW_{(i,ii)}$ (Eq. 9) when using the approximation of (ii) η primarily reflecting the 1^{st} baroclinic mode ($\alpha_n \sim \alpha_1 \sim 1$), such as :

$$EPW_{(i,ii)} = \underbrace{-\frac{\beta\rho_0 g^2}{2f^2}\frac{\partial}{\partial x}\left(\frac{\int_{-H}^{\eta}\phi_1^2\,dz}{|\phi_1^2|_{z=0}}\eta'^2\right)}_{\beta-contribution\ (\mathbf{A1})} + \underbrace{\frac{\beta\rho_0 g^2}{2f^2}\frac{\partial H}{\partial x}\frac{|\phi_1^2|_{z=-H}}{|\phi_1^2|_{z=0}}\eta'^2}_{\beta-contribution\ to\ topographic\ interactions\ (\mathbf{A2})} + \underbrace{\frac{\rho_0 g^2}{2f}\nabla_H H\cdot|\mathbf{k}\wedge\nabla_H\left(\frac{\phi_1^2}{|\phi_1^2|_{z=0}}\right)\eta'^2|_{z=-H}}_{EKE\ flux-topographic\ interactions\ (\mathbf{C})} \tag{9}$$

2.3.3 Approximation (iii) ($EPW_{(i,ii,iii)}$ and $EPW_{(i,iii)}$)

$EPW_{(i,ii)}$ (Eq. 9) can be written as $EPW_{(i,ii,iii)}$ (Eq. 10) when using the approximation of (iii) topographic interactions (**A2**, **C**) being negligible compared to the β-contribution (**A1**), such that :

$$EPW_{(i,ii,iii)} = \underbrace{-\frac{\beta\rho_0 g^2}{2f^2}\frac{\partial}{\partial x}\left(\frac{\int_{-H}^{\eta}\phi_1^2\,dz}{|\phi_1^2|_{z=0}}\eta'^2\right)}_{\beta-contribution\ (\mathbf{A1})} \tag{10}$$

The expression of $EPW_{(i,ii,iii)}$ (Eq. 10) corresponds to the contribution of linear EKE flux, driven by the β-effect, acting on the 1^{st} baroclinic mode to the true EPW (Zhai et al., 2010).
We additionally define $EPW_{(i,iii)}$ (Eq. 11), which is equivalent to $EPW_{(i,ii,iii)}$ (Eq. 10) with approximation (ii) relaxed, such that :

$$EPW_{(i,iii)} = \underbrace{-\frac{\beta\rho_0 g^2}{2f^2}\frac{\partial}{\partial x}\left(\frac{\int_{-H}^{\eta}\phi_n^2\,dz}{|\phi_n^2|_{z=0}}\alpha_n^2\eta'^2\right)}_{\beta-contribution\ (\mathbf{A1})} \tag{11}$$

In the following sections, we will test if $EPW_{(i,ii,iii)}$ (Eq. 10) and $AEKE_{(i)}$ (Eq. 8) are reliable approximations of EPW (Eq. 4) (section 4) and $AEKE$ (Eq. 4) (section 5), respectively. The main terms discussed in these sections are summarized in Table 1. Beforehand, section 3 presents the methods and data.

3 Method

3.1 Observations and numerical model

We first present the observations and the regional numerical simulation used in this study. We then assess the sensitivity of the paradigm of mesoscale eddy decay at the Agulhas Current region, by comparing the observed and modeled $EPW_{(i,ii,iii)}$ (Eq. 10). The

Table 1: Summary of the true and η-based expressions of the eddy-pressure work (EPW) and advection of mesoscale EKE by the total flow ($AEKE$) constituting the mesoscale EKE ($EKE_{n=0-1}$)-flux divergence.

Acronym	Expression	Description
EPW (Eq. 5)	$\nabla_H \cdot \int_{-H}^{\eta} \mathbf{u'}_n p'_n \phi_n^2 \, dz$	true mesoscale eddy-pressure work
$EPW_{(i)}$ (Eq. 7)	$-\frac{\beta\rho_0 g^2}{2f^2}\frac{\partial}{\partial x}\left(\frac{\int_{-H}^{\eta}\phi_n^2 \, dz}{\lvert\phi_n^2\rvert_{z=0}}\alpha_n^2\eta'^2\right)$ $+\frac{\beta\rho_0 g^2}{2f^2}\frac{\partial H}{\partial x}\frac{\lvert\phi_n^2\rvert_{z=-H}}{\lvert\phi_n^2\rvert_{z=0}}\alpha_n^2\eta'^2$ $+\frac{\rho_0 g^2}{2f}\nabla_H H\cdot\lvert\mathbf{k}\wedge\nabla_H\left(\frac{\phi_n^2}{\lvert\phi_n^2\rvert_{z=0}}\right)\alpha_n^2\eta'^2\rvert_{z=-H}$, with $\alpha_n=\frac{\eta'_n}{\eta'}$	η-based mesoscale eddy-pressure work using approximation (i)
$EPW_{(i,ii,iii)}$ (Eq. 10)	$-\frac{\beta\rho_0 g^2}{2f^2}\frac{\partial}{\partial x}\left(\frac{\int_{-H}^{\eta}\phi_1^2 \, dz}{\lvert\phi_1^2\rvert_{z=0}}\eta'^2\right)$	η-based mesoscale eddy-pressure work using approximations (i), (ii) and (iii)
$EPW_{(i,iii)}$ (Eq. 11)	$\frac{\beta\rho_0 g^2}{2f^2}\frac{\partial}{\partial x}\left(\frac{\int_{-H}^{\eta}\phi_n^2 \, dz}{\lvert\phi_n^2\rvert_{z=0}}\alpha_n^2\eta'^2\right)$, with $\alpha_n=\frac{\eta'_n}{\eta'}$	η-based mesoscale eddy-pressure work using approximation (i) and (iii)
$AEKE$ (Eq. 6)	$\frac{\rho_0}{2}\nabla_H \cdot \int_{-H}^{\eta} \mathbf{u}_n\phi_n \lvert\lvert\mathbf{u}'_n\phi_n\rvert\rvert^2 \, dz$	true advection of mesoscale EKE by the total flow
$AEKE_{(i)}$ (Eq. 8)	$-\frac{\beta\rho_0 g}{2f^2}\int_{-H}^{\eta}\lvert\lvert\mathbf{u}'_{g,n}\phi_n\rvert\rvert^2\partial x(\frac{\phi_n}{\lvert\phi_n\rvert_{z=0}}\lambda_n\eta) \, dz$ $+\frac{\rho_0}{2}\int_{-H}^{\eta}(\mathbf{u}_{g,n}\phi_n)\cdot\nabla_H\lvert\lvert\mathbf{u}'_{g,n}\phi_n\rvert\rvert^2 \, dz$ $+\frac{\rho_0}{2}\nabla_H H\cdot\lvert\mathbf{u}_{g,n}\phi_n\rvert\lvert\mathbf{u}'_{g,n}\phi_n\rvert\rvert^2\rvert_{z=-H}$, with $\lambda_n=\frac{\eta_n}{\eta}$	η-based advection of mesoscale EKE by the total flow using approximation (i)

term requires vertical modes (derived using a time-averaged stratification N^2) and η fields.

3.1.1 Observations

The WOCE (World Ocean Circulation Experiment) and WOA18 (World Ocean Atlas) climatologies provide *in situ* temperature and salinity fields at a global scale, with respective horizontal resolutions of 1/2° and 1°, for monthly compositing means (Gouretski & Koltermann, 2004; Locarnini et al., 2018; Zweng et al., 2019). Vertical modes are derived from the time-averaged stratification, computed from temperature and salinity provided by both climatologies. Altimetric data are mapped on a regular 1/4°- and 1/3°-grid by AVISO (Archiving, Validation and Interpretation of Satellite Oceanographic data) and provide η field for weekly compositing means at a global scale. Here we focus on a subset of data over the Agulhas Current region (15°E - 34°E and 27°S - 40°S) for the 1995-2004 period.

3.1.2 Numerical model

A regional numerical simulation of the Agulhas Current was performed using the Coastal and Regional COmmunity (CROCO) model. It is a free surface model, based on ROMS (Shchepetkin & McWilliams, 2005), which solves the primitive equations in the Boussinesq and hydrostatic approximations using a terrain following coordinate system (Debreu et al., 2012). The simulation has a horizontal resolution of dx $\sim$ 2.5 km and 60 vertical levels. It encompasses the Agulhas Current region from its source, north of the Natal Bight (27°S), to the Agulhas Retroflection ($\sim$ 37°S), from where it becomes the Agulhas Return Current and flows eastward. Boundary conditions are supplied by two lower-resolution grids (dx $\sim$ 22.5 km and 7.5 km, respectively covering most of the South Indian Ocean and its western part). The surface forcing is provided by a bulk-formulation using daily relative winds. The regional numerical simulation settings and modeled mesoscale eddy dynamics are presented in details by Tedesco et al. (2019, 2022). Here vertical modes are derived from the time-averaged stratification over the 1995-2004 period, computed from the modeled temperature and salinity.

3.2 $EPW_{(i,ii,iii)}$ from observations and a numerical model

In order to ensure the ability of the model to reproduce a realistic mesoscale eddy dynamics and to assess the sensitivity of the paradigm of mesoscale eddy decay at the Agulhas Current region, we compare $EPW_{(i,ii,iii)}$ (Eq. 10) computed from observations (as in Zhai et al. (2010)) and from the model (Figure 1).

Observed and modeled $EPW_{(i,ii,iii)}$ are in fairly good agreement across the domain of the dx $\sim$ 2.5 km grid. Both $EPW_{(i,ii,iii)}$ are most intense at the Retroflection and along the Agulhas Return Current (O(0.1-0.5) W m^{-2}) and are less intense along the Agulhas Current and in the Subgyre (O(0.01-0.1) W m^{-2}). However, the Agulhas Current region – from north of the Natal Bight ($\sim$ 27°S) to the African tip ($\sim$ 37°S) and from the shelf to about 150 km offshore, a typical width of western boundary currents (black region in Figure 1) – stands out for both. In this region, $EPW_{(i,ii,iii)}$ is almost uniformly negative and has a cumulative net negative contribution of magnitude $O(1)$ GW. The negative $EPW_{(i,ii,iii)}$ along the Agulhas Current – referred to as the Western Boundary (WB) region in the following – is consistent with the hotspot of net EKE sink in the region near the western boundary of the South Indian Ocean (poleward of 10°S) suggested by Zhai et al. (2010).

The main discrepancy between the observed and modeled $EPW_{(i,ii,iii)}$ is the magnitude of the cumulative EKE sinks in the WB region. There is roughly a twofold decrease in the model compared to observations (Figure 1a,b,c). The magnitude difference is still

present when using smoothed η, with a length scale of 100 km, in the model to mimic the altimetry data processing done by AVISO (Figure 1d). It indicates that the EKE sink in the WB region is robust to altimetry data processing and that horizontal scales $< O(100)$ km do not significantly contribute to the $EPW_{(i,ii,iii)}$ term. Using different climatologies (1/2° WOCE or 1° WOA18) and satellite altimetry data of different resolutions (1/4° or 1/3° AVISO) also does not significantly change the result (Figure 1a,b).

The magnitude difference is unlikely explained by the forcing of eddies generated in the parent nest that would propagate in the dx $\sim$ 2.5 km grid. The grid is forced at each time step at the boundaries by a parent grid (dx $\sim$ 7.5 km), which resolves mesoscale eddies of scales $<$ 100 km. An explanation can be the slight underestimation of the surface EKE reservoir in the dx $\sim$ 2.5 km simulation, compared to AVISO, in the Subgyre region (Figure 2 in Tedesco et al. (2022)). A weaker EKE reservoir can lead to a weaker spatial redistribution of the EKE (EKE flux divergence). It is supported by the observed $EPW_{(i,ii,iii)}$ showing slightly larger magnitudes (-0.1 W m^{-2}) than the modeled $EPW_{(i,ii,iii)}$ (-0.05 W m^{-2}), in the same areas where the surface AVISO-based EKE is slightly larger (0.05 m^2 s^{-2}) than the modeled one ($>$ 0.03 m^2 s^{-2}). Another explanation can be the definition of the WB region. The uniform EKE sink denoted by $EPW_{(i,ii,iii)}$ has a larger extension in the observations than in the model (Figure 1). With a typical width of western boundary currents, the WB region fully encompasses the modeled uniform EKE sink, with the southern face closely following the $O(0)$ W m^{-1} isoline. However, the WB region encompasses most, but not all of the observed uniform EKE sink.

Both observed and modeled $EPW_{(i,ii,iii)}$ are mainly negative in the WB region, showing a net EKE sink. It is consistent with the paradigm of the decay of remotely-generated mesoscale eddy at western boundaries (Zhai et al., 2010). It also ensures that the dx $\sim$ 2.5 km numerical simulation reproduces a realistic mesoscale eddy dynamics and confirms its use to assess the η-based diagnostic of EKE flux divergence in the WB region.

4 Results I : Validity of the approximated $EPW_{(i,ii,iii)}$ and main contributions to the true EPW

In this section we evaluate the η-based estimate of EPW ($EPW_{(i,ii,iii)}$). We first evaluate if $EPW_{(i,ii,iii)}$ (Eq. 10) is a reliable approximation of the true EPW (Eq. 4). We then evaluate separately the impacts of approximations (i), (ii) and (iii) (cf. section 2.1.3) and characterize what are the main contributions to the true EPW.

4.1 Comparison between approximated $EPW_{(i,ii,iii)}$ and true EPW

$EPW_{(i,ii,iii)}$ and EPW in Figure 2 – and in all the following Figures – have been smoothed using a 75 km-radius Gaussian kernel. Smoothed terms emphasize the large-scale patterns driving the cumulative contributions of EPW in the WB region and ease the comparison with $EPW_{(i,ii,iii)}$. The smoothing length scale corresponds to a typical mesoscale eddy radius at mid-latitudes, as inferred from satellite altimetry (Chelton et al., 2011). The sensitivity of the EPW term to the smoothing length scale is presented in Appendix A.

$EPW_{(i,ii,iii)}$ and EPW strongly differ by their patterns across the whole domain and by their cumulative contributions in the WB region (Figures 2a and b). $EPW_{(i,ii,iii)}$ is mainly negative in the WB region (-1.10 GW; Figure 2a) and EPW is mainly positive (0.81 GW; Figure 2b).

EPW shows contrasted net mesoscale EKE sources and sinks within the WB region, consistent with the documented Agulhas Current mesoscale variability (Lutjeharms, 2006;

Paldor & Lutjeharms, 2009; Tedesco et al., 2022). Along the northern and stable Agulhas Current branch (upstream of Port Elizabeth), EPW is negative (O(-0.01) W m^{-2}), except at the Natal Bight ($\sim 31°$E) where EPW is positive and Natal Pulses are locally generated (Elipot & Beal, 2015). Along the southern and unstable current branch (downstream of Port Elizabeth), EPW is positive over the entire width of the WB region, except at the Agulhas Bank tip ($\sim 23°$E) where mesoscale EKE is locally lost. The cumulative contribution of EPW across the WB region is dominated by the net mesoscale EKE sources ($EPW > 0$), which are the most intense along the southern current branch where mesoscale variability is high. The locally gained mesoscale EKE is transported downstream. It mainly exits the WB region by its western face toward the South-East Atlantic Ocean or entering back the South Indian Ocean following the Agulhas Return Current (vector fields in Figure 2b).

The negative $EPW_{(i,ii,iii)}$ and the positive EPW support opposite paradigms of mesoscale eddy dynamics in the WB region. The η-based version is dominated by a local decay of remotely-generated mesoscale eddies, while the true version is dominated by a local generation of mesoscale eddies, which are then exported downstream. It indicates that $EPW_{(i,ii,iii)}$ (Eq. 10) – β-contribution acting on the 1^{st} baroclinic mode – does not represent the main contribution to the true EPW (Eq. 5). This suggests that the contribution of β-effect acting on the 1^{st} baroclinic mode is counterbalanced by other dynamical processes to produce a positive EPW in the WB region. We investigate in the following which of the approximations (i), (ii) and (iii) limits the η-based diagnostic of EPW.

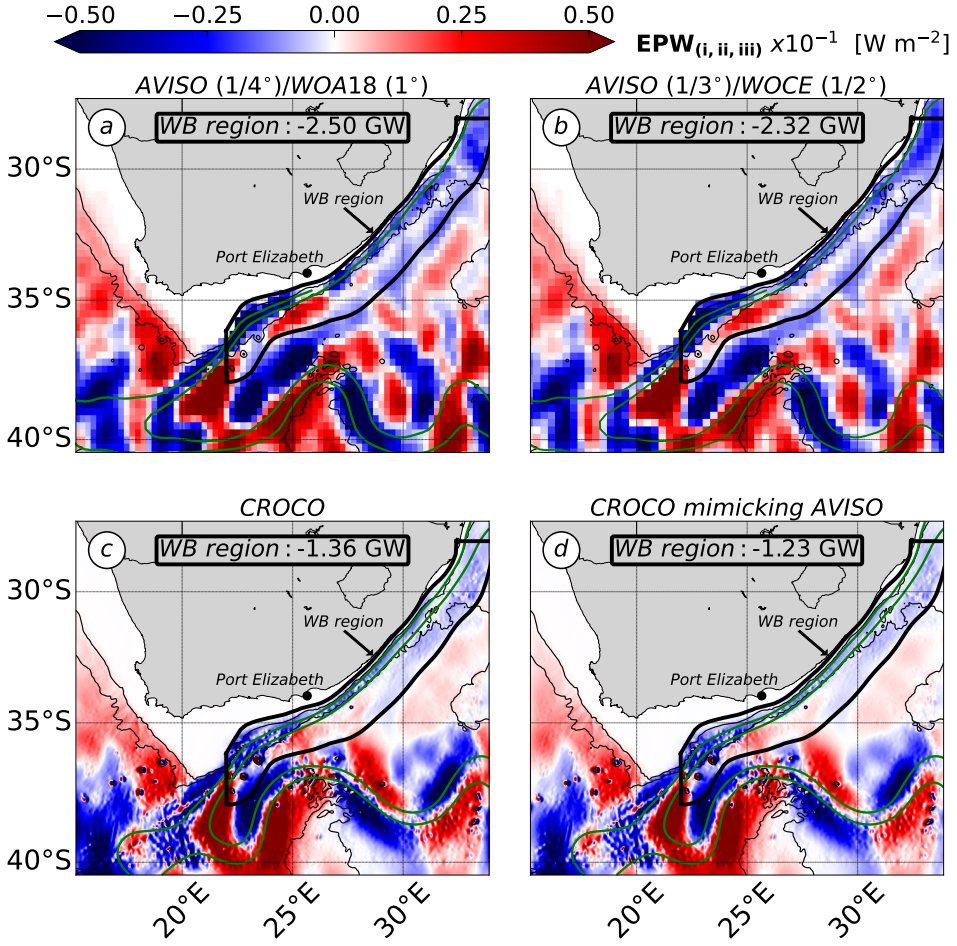

Figure 1: $EPW_{(i,ii,iii)}$ (Eq. 10) [W m^{-2}] for (a) AVISO new products (1/4°) and WOA18 (1°) climatology, (b) AVISO old products (1/3°) and WOCE (1/2°) climatology, (c) CROCO (dx $\sim$ 2.5 km) and (d) CROCO mimicking AVISO processing (η fields smoothed with a 50 km-radius Gaussian kernel). Terms are averaged over the 1995-2004 period. The black area denotes the WB region and the terms integral in the region are in [GW] (10^9 W). The green contours denote the 0.25 m and 0.5 m isolines of time-averaged η and the black contours denote the 1000 m and 3000 m isobaths. (d) Small scales patterns, visible in spite of the smoothed η fields, are due to horizontal gradients of the 1^{st} baroclinic mode which is at the model resolution (dx $\sim$ 2.5 km). All $EPW_{(i,ii,iii)}$ show, in good agreement, a net mesoscale EKE sink in the WB region ($EPW_{(i,ii,iii)} < 0$). It is consistent with the paradigm of the decay of remotely-generated mesoscale eddies at western boundaries (Zhai et al., 2010).

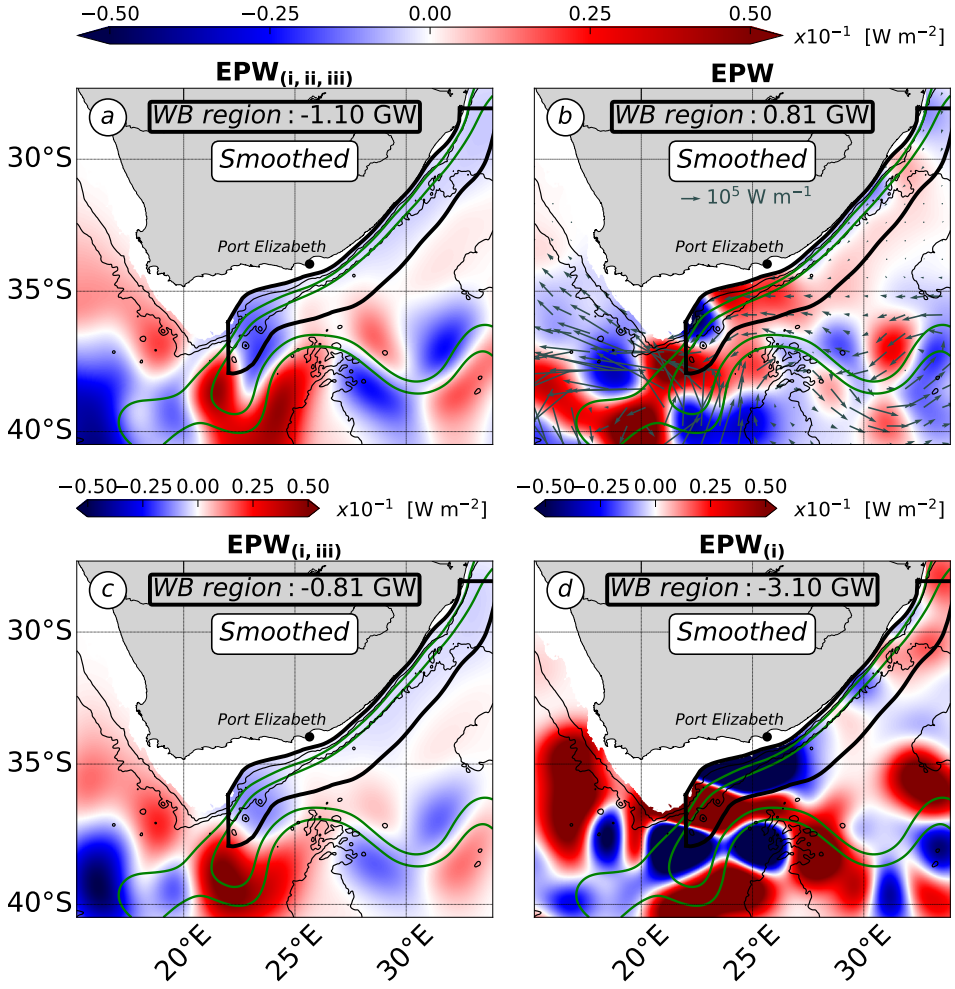

Figure 2: (a) $EPW_{(i,ii,iii)}$ (Eq. 10), (b) EPW (Eq. 5), (c) $EPW_{(i,iii)}$ (Eq. 11) and (d) $EPW_{(i)}$ (Eq. 7) [W m^{-2}]. Terms are smoothed with a 75 km-radius Gaussian kernel. (b) Vector fields denote the mesoscale EKE flux ($\int_{-H}^{\eta} \mathbf{u}'_n p'_n \phi_n^2 \, dz$ with $n = 0 - 1$) [W m^{-1}]. (cf. Figure 1 for a detailed caption). The black area denotes the WB region and the terms integral in this region are in [GW] (10^9 W). The green contours denote the 0.25 m and 0.5 m isolines of time-averaged η and black contours denote the 1000 m and 3000 m isobaths. (a) and (b) strongly differ ($EPW_{(i,ii,iii)} < 0$ and $EPW > 0$ in the WB region), indicating that $EPW_{(i,ii,iii)}$ is not a reliable estimate of the true mesoscale EPW. (a) and (c) results from different contributions of the barotropic and 1^{st} baroclinic modes, indicating that approximation (ii) biases the interpretation of $EPW_{(i,ii,iii)}$. (c) and (d) differs, invalidating approximation (iii) for the η-based EPW.

4.2 Approximation (ii) : contribution of the barotropic mode ($EPW_{(i,ii,iii)}$ *vs.* $EPW_{(i,iii)}$)

With approximation (ii) (η field primarily reflecting the 1^{st} baroclinic mode), the mesoscale EKE reservoir – formally represented by the barotropic and 1^{st} baroclinic modes (Wunsch, 2007; Smith & Vallis, 2001; Venaille et al., 2011; Tedesco et al., 2022) – is represented by the 1^{st} baroclinic mode alone. This can lead to a misinterpretation of the dynamics of the mesoscale EKE reservoir. It can gain or loose EKE through the barotropic mode and the barotropic and 1^{st} baroclinic modes can exchange EKE, via barotropisation and scattering processes, without affecting the content of the mesoscale EKE reservoir. The importance of barotropization has been shown in the WB region of the North Indian Ocean (Vic et al., 2014). The necessity to account for both modes to infer the mesoscale EKE flux divergence in the WB region is supported by the true EPW. Its net contribution in the WB region (0.81 GW; Figure 2b) results from the partial compensation between the barotropic (1.56 GW) and the 1^{st} baroclinic modes (-0.75 GW) (not shown), indicating that barotropization is a significant process in the region.

The expression of $EPW_{(i,iii)}$ (Eq. 11) accounts for the different vertical modes using α_n^2 – the vertical partitioning of the η variance. The η variance mainly partitions into the 1^{st} baroclinic mode (38 $\pm$ 2 %) and more weakly, but still significantly, into the barotropic mode (16 $\pm$ 4 %) (Appendix B). It indicates that the mesoscale EKE reservoir can be formally represented by the barotropic and 1^{st} baroclinic modes using η. The η variance also significantly partitions into an intermodal coupling term (36 $\pm$ 2 %), originating from the modal correlation in time at the surface (Wunsch, 1997). However, the intermodal coupling term does not contribute to $EPW_{(i,iii)}$ (Eq. 11), which uses the orthogonality contribution (2) and only accounts for individual vertical modes.

Approximation (ii) is evaluated by comparing $EPW_{(i,ii,iii)}$ (Figure 2a) with $EPW_{(i,iii)}$ (Figure 2c). $EPW_{(i,ii,iii)}$ and $EPW_{(i,iii)}$ have highly similar patterns and magnitudes across the region. However, the net mesoscale EKE sink in the WB region denoted by $EPW_{(i,iii)}$ (-0.81 GW; Figure 2c) results from the combination of the barotropic (-0.51 GW) and 1^{st} baroclinic modes (-0.30 GW). It contrasts with the net EKE sink denoted by $EPW_{(i)}$ (-1.10 GW), attributable to the 1^{st} baroclinic mode alone (Figure 2a). This indicates that both vertical modes are needed to accurately interpret the mesoscale EPW. It also indicates that even though the barotropic mode does not dominate the η variance (16 $\pm$ 4 %; Appendix B), it is the main contribution to the vertically-integrated $EPW_{(i,iii)}$ in the WB region.

Approximation (ii) biases the interpretation of the η-based EPW ($EPW_{(i,ii,iii)}$ in Eq. 10), because the barotropic mode represents the main contribution to the net EKE sink in the WB region denoted by $EPW_{(i,iii)}$ (Eq. 11). However, it is not at the origin of the strong discrepancies between the η-based terms - $EPW_{(i,ii,iii)}$ (Eq. 10) and $EPW_{(i,iii)}$ (Eq. 11) - and the true EPW (Eq. 4).

4.3 Approximation (iii) : contribution of topographic interactions ($EPW_{(i,iii)}$ *vs.* $EPW_{(i)}$)

The WB region is characterized by large topographic variations, having a spatially-averaged magnitude of 3 10^{-2}, which can locally peak at 6 10^{-2}. This questions the use of approximation (iii) of EKE flux-topographic interactions to be negligible in the WB region.

Approximation (iii) is evaluated by comparing $EPW_{(i,iii)}$ (Eq. 11; Figure 2c) against $EPW_{(i)}$ (Eq. 7; Figure 2d) which includes topographic interactions. The two terms locally differ by their patterns and magnitudes. However, their cumulative contributions in the WB region show a net mesoscale EKE sink ($EPW_{(i,iii)}$;$EPW_{(i)} < 0$). $EPW_{(i)}$, including topographic interactions, has contrasted patterns within the WB region and is the most intense at the Eastern Agulhas Bank Bight (23°E-27°E). Its local magnitude is larger by an order of magnitude than that of $EPW_{(i,iii)}$, excluding topographic interactions.

Topographic interactions are mainly due to the term of EKE flux-topographic interactions (**C** : -3.05 GW in the WB region, not shown), because the term of β-contribution to topographic interactions has a negligible contribution (**A2** : 0.76 GW in the WB region, not shown). A valid approximation would be to neglect the β-contribution (**A1**) and the β-contribution to the topographic interactions (**A2**) compared to the EKE flux-topographic interactions (**C**).

Approximation (iii) has a significant impact on $EPW_{(i,iii)}$ (Eq. 11). However, $EPW_{(i)}$ (Eq. 7) – adjusted of approximations (ii) and (iii) – is mainly negative in the WB region, consistently with the former version of the η-based EPW ($EPW_{(i,ii,iii)}$ in Eq. 10). It indicates that approximations (ii) and (iii) are not the reasons for the opposite signs in the WB region between the η-based ($EPW_{(i,ii,iii)}$ in Eq. 10; Figure 2a) and the true EPW (EPW in Eq. 4; Figure 2b).

4.4 Approximation (i) : contribution of ageostrophic motions (β-contribution *vs.* ageostrophic EPW)

Approximation (i) of geostrophic velocities is the last possible reason for the opposite signs of the η-based ($EPW_{(i,iii)}, EPW_{(i)} < 0$; Figure 2c,d) and true EPW ($EPW > 0$; Figure 2b) in the WB region. It suggests that the main contribution to the true mesoscale EPW is the ageostrophic part of mesoscale eddies velocity.

We use a scale analysis to explain the prevalence of ageostrophy, compared to the β-contribution (in $EPW_{(i)}$; Eq. 7 and $EPW_{(i,iii)}$; Eq. 11), for the true EPW (Eq. 4). We focus here on the β-contribution only, because it was the one investigated as the main contribution to the true EPW by Zhai et al. (2010). The decomposition of velocity and pressure into a geostrophic and an ageostrophic part in the modal EKE equation (Eq. 4), results in three types of contribution to EPW: a purely geostrophic one (β-contribution to EPW_i; Eq. 7), a purely ageostrophic one ($\mathbf{u}'_{ag,n}$; $p'_{ag,n}$), and a coupled geostrophic-ageostrophic one ($\mathbf{u}'_{ag,n}$; $p'_{g,n}$). We derive the scale analysis for the purely ageostrophic (Eq. 12) and partially ageostrophic (Eq. 13) terms to assess their contribution to the true EPW.

$$\left| \int_{-H}^{\eta} \nabla_H \cdot \left(\mathbf{u}'_{ag,n} p'_{ag,n} \phi_n^2 \right) \, dz \right| \sim \frac{Ro^2 U'_g P'_g H}{L} \tag{12}$$

$$\left| \int_{-H}^{\eta} \nabla_H \cdot \left(\mathbf{u}'_{ag,n} p'_{g,n} \phi_n^2 \right) \, dz \right| \sim \frac{Ro U'_g P'_g H}{L} \tag{13}$$

$$\left| \frac{\beta \rho_0 g^2}{2 f^2} \int_H^{\eta} \frac{\partial}{\partial x} \left(\frac{\phi_n^2}{|\phi_n^2|_{z=0}} \alpha_n^2 \eta'^2 \right) \, dz \right| \sim \frac{\widehat{\beta} P' U'_g H}{\widehat{f}} \tag{14}$$

$$\frac{(12)}{(14)} = \frac{Ro^2 \widehat{f}}{L \widehat{\beta}} = \frac{\widehat{\zeta'_{RMS}}^2}{L \widehat{f} \widehat{\beta}} = \frac{L_{cross-over}}{L}, \text{ with } L_{cross-over} = \frac{\widehat{\zeta'_{RMS}}^2}{\widehat{f} \widehat{\beta}} \tag{15}$$

$$\frac{(13)}{(14)} = \frac{Ro \widehat{f}}{L \widehat{\beta}} = \frac{\widehat{\zeta'_{RMS}}}{L \widehat{\beta}} = \frac{L_{cross-over}}{L}, \text{ with } L_{cross-over} = \frac{\widehat{\zeta'_{RMS}}}{\widehat{\beta}} \tag{16}$$

with $|\nabla_H, \frac{\partial}{\partial x}| \sim \frac{1}{L}$, $|\int_{-H}^{\eta} < . > dz| \sim H$, $|\beta| \sim \widehat{\beta}$, $|f| \sim \widehat{f}$, $|\mathbf{u}'_{ag,n}| \sim RoU'_g$ and $|p'_{ag,n}| \sim RoP'_g$ using the expansion of velocity and eddy pressure with Ro the small parameter – defined as the vertical average of the root mean square of the normalized relative vorticity of mesoscale eddies ($\zeta' = \partial_x v' - \partial_y u'$), such as : $Ro = \left| \frac{1}{H} \int_{-H}^{\eta} \left(\frac{\zeta'_{RMS}}{f} \right) \, dz \right| \sim \frac{\widehat{\zeta'_{RMS}}}{\widehat{f}}$ – $|p'_{g,n}| \sim P'_g \sim \rho_0 \widehat{f} U'_g L$ using geostrophy and $\left| \frac{\phi_n^2 \alpha_n^2 \eta'^2}{|\phi_n^2|_{z=0}} \right| \sim \frac{P'_g U'_g L \widehat{f}}{\rho_0 g^2}$ using the hydrostatic approximation and geostrophy.

The scale analysis leads to the definition of a cross-over scale ($L_{cross-over}$ in Eq. 15 and 16) marking the transition from an ageostrophic-dominated EPW ($L_{cross-over} >> L_{eddy}$) to a β-effect dominated EPW ($L_{cross-over} << L_{eddy}$). It must be noted that the definition of $L_{cross-over}$ is not unique. An equivalent expression can be obtained by using $Ro = \frac{U'}{fL}$, such that : $\frac{(13)}{(14)} = \frac{U'}{L^2 \widehat{\beta}} = \frac{L_{cross-over}^2}{L^2}$, with $L_{cross-over} = \sqrt{\frac{U'}{\widehat{\beta}}} = Rh$. Rh is the Rhines scale defined in turbulence geostrophic theory to mark the transition from an advectively-dominated ($Rh << L_{eddy}$) to a Rossby waves-dominated ($Rh >> L_{eddy}$) turbulent regime (Rhines, 1975). We discuss here $Ro = \frac{\zeta'_{RMS}}{f}$ (Figure 3a) and the corresponding scale ratio $\frac{L_{cross-over}}{L}$ (Eq. 12; Figure 3b and Eq. 13; not shown). Rh is assessed for comparison in Appendix C.

Ro is a measure of ageostrophy (Cushman-Roisin & Beckers, 2011). The typical range of Ro values for mesoscale eddies at mid-latitudes, inferred from satellite altimetry data ($O(< 0.05)$ from Chelton et al. (2011)), is used as a reference for mesoscale eddies in the WB region. Ro has a contrasted distribution in the WB region (Figure 3a). 70 % of its values are in the range $O(0.02$ - $0.07)$. The rest of the values are larger ($O(0.07$-$0.65)$) and located at the Agulhas Current inner front. It confirms that mesoscale eddies are mainly geostrophic in most of the WB region. They are more ageostrophic at the inner front where the velocity shear is more intense and where they likely interact with topography.

Although geostrophy is a good approximation for mesoscale eddies velocity in most of the WB region (Figure 3a), the purely geostrophic EPW – corresponding to a β-contribution (Figures 2a,c) – is not the main contribution to the true mesoscale EPW (Figures 2b). For the case of a partially ageostrophic EPW ($L_{cross-over}$ in Eq. 13), $L_{cross-over} \sim O(3-7)Rd$ in 70 % of the WB region, with larger ratio ($L_{cross-over} \sim O(7-19)Rd$) located at the inner front of the Agulhas Current (Figure 3b). It indicates that the partially ageostrophic EPW dominates the β-effect for the mesoscale regime in the WB region. The partially ageostrophic-dominated EPW is also supported by the equivalent expression of $L_{cross-over}$ depending on Rh (Appendix C). A typical radius of mesoscale eddies at mid-latitudes, inferred by satellite altimetry, is 75 km (Chelton et al., 2011). With $L_{cross-over} = O(105$-

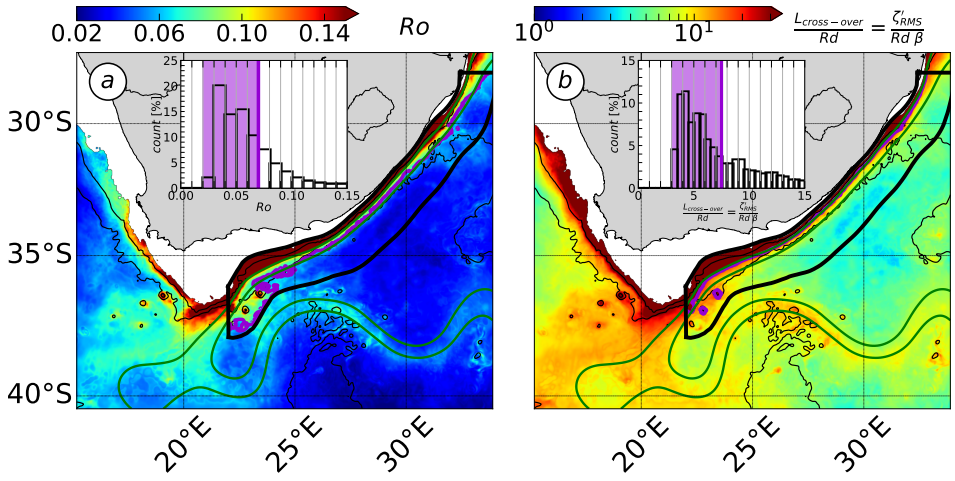

Figure 3: (a) Ro for mesoscale eddies ($Ro = \frac{\zeta'_{RMS}}{f}$, with ζ' the normalized relative vorticity) and (b) $\frac{L_{cross-over}}{Rd} = \frac{\zeta'_{RMS}}{Rd\ \beta}$ defined for the partially ageostrophic EPW (Eq. 16). The purple lines denote Ro and $\frac{L_{cross-over}}{Rd}$ 70 % percentiles, the green contours denote the 0.25 m and 0.5 m isolines of time-averaged η and black contours denote the 1000 m and 3000 m isobaths. The terms count in the WB region [%] are shown as barplots, where purple shaded areas denote the 70 % percentile range of values. (a) Ro shows that mesoscale eddies are mainly geostrophic in the WB region (O(0.02-0.07) in 70 % of the WB region). However, (b) $\frac{L_{cross-over}}{Rd} >> 1$ in the WB region, resulting in L_{eddy} ($\geq Rd$) to fall in the range of partially ageostrophic-dominated EPW, compared to the β-effect.

256) km in 70 % of the WB region (not shown), the β-effect would be the main contribution to the true mesoscale EPW for the large-scale range of mesoscale eddies. For the case of a purely ageostrophic EPW ($L_{cross-over}$ in Eq. 12), $L_{cross-over} \sim O(0.1 - 0.5)Rd$ in 70 % of the WB region with larger ratio located at the inner front of the Agulhas Current (not shown). It indicates that the β-effect dominates the purely ageostrophic EPW for the mesoscale regime in the WB region.

In a nutshell, the main contribution to the true mesoscale EPW takes the form of a coupled geostrophic (pressure) and ageostrophic (velocity) EPW in the WB region ($L_{cross-over} >> L_{eddy}$ from Eq. 13). Approximation (i) therefore questions the use of satellite altimetry data to infer EPW (Eq. 5). In order to conclude on the use of satellite altimetry data to infer the EKE flux divergence, we assess in the following section the impact of the geostrophic approximation (i) on the $AEKE$ term.

5 Results II : Main contributions to the true $AEKE$

In this section we evaluate the η-based estimate of $AEKE$ ($AEKE_{(i)}$). We first evaluate if $AEKE_{(i)}$ (Eq. 8) is a reliable approximation of $AEKE$ (Eq. 4). We then characterize the main contributions to the true $AEKE$.

5.1 Comparison between approximated $AEKE_{(i)}$ and true $AEKE$

$AEKE_{(i)}$ and $AEKE$ are in fairly good agreement across the whole domain (Figure 4a,b). They are mainly positive in the WB region, supporting the WB region as the place of mesoscale eddy generation whose energy is then exported. Both $AEKE$ are the most intense along the southern Agulhas Current branch (downstream of Port Elizabeth), where mesoscale variability is high. Along this portion of the current, the net mesoscale EKE sources spread almost uniformly across the width of the WB region. The net mesoscale EKE source cumulated in the WB region shown by $AEKE_{(i)}$, amounts to 73 % of the one shown by $AEKE$. The weaker magnitude is explained by the presence of a large sink at the Eastern Agulhas Bank Bight Tip (22°E - 23°E) visible in $AEKE_{(i)}$.

The fairly good qualitative and quantitative agreements between $AEKE_{(i)}$ and the true $AEKE$ indicate that the η-based term is a reliable estimate of $AEKE$. It subsequently indicates that the approximation (i) of geostrophy is valid for $AEKE$, in contrast with EPW (section 4.4) and consistently with Ro (Figure 3a). In the following subsection, we characterize in details the contribution of each sub-components – β-contribution (**A** in Eq. 8), work of eddy-total flow interactions (**B** in Eq. 8) and EKE flux-topographic interactions (**C** in Eq. 8) – to $\mathbf{AEKE_{(i)}}$ (Eq. 8).

On a separate note, both terms result from a combination of the barotropic ($AEKE_{(i)}$: 0.57 GW ; $AEKE$: 0.88 GW, not shown) and 1^{st} baroclinic modes ($AEKE_{(i)}$: 1.10 GW ; $AEKE$: 1.41 GW, not shown). It confirms the need to consider both vertical modes to accurately infer the mesoscale EKE flux divergence in the WB region.

5.2 Approximation (i) : contribution of geostrophic motions to the true $AEKE$

The work of eddy-total flow interactions (**B** in Figure 4d) represents the main contribution to $AEKE_{(i)}$ (Figure 4a) and the β-contribution (**A** in Figure 4c) has a weaker and opposite contribution.

The work of eddy-total flow interactions (**B** in Eq. 8) is a reliable estimate of the net mesoscale EKE source in the WB region denoted by $AEKE_{(i)}$ (up to 73 %) and by $AEKE$ (up to 53 %). The β-contribution (**A** in Eq. 8) is almost uniformly negative in the WB region and amounts for a cumulated net mesoscale EKE sink of -0.19 GW. **A** in $AEKE$ (Eq. 8) is the nonlinear counterpart of the β-contribution to EPW (**A** term in Eq. 7). Both β-terms have similar contributions to the EKE flux divergence (Figures 2c and 4c), although the nonlinear β-term has a weaker cumulative contribution in the WB region (-0.19 GW; Figure 4c) than the linear β-term (-0.81 GW; Figure 2c). The cumulative contribution in the WB region of EKE flux-interactions with topography (**C** in Eq. 8) is 0.65 GW (not shown). It is weaker than the work of eddy-total flow interactions (**B**), but remains significant. It confirms the need to account for topographic interactions to accurately infer the net mesoscale EKE sources and sinks in the WB region.

6 Conclusion on the η-based EKE flux divergence

In this section, we draw a conclusion on the use of η to infer the EKE flux divergence, based on our results for the EPW (cf. section 4) and $AEKE$ components (cf. section 5).

The EKE flux divergence shows a net mesoscale EKE source in the WB region ($EPW > 0$ in Figure 2b; $AEKE > 0$ in Figure 3b), supporting the WB as a region of mesoscale eddies generation. The net mesoscale EKE source in the WB region (3.10 GW) is mainly due to $AEKE$ (2.29 GW) and more weakly to EPW (0.81 GW).

$AEKE$ corresponds to the advection of EKE by the total flow. It significantly exports EKE along the southern Agulhas Current branch ($AEKE > 0$), where mesoscale variability is high (Figure 4b). $AEKE$ is dominated by geostrophic EKE flux (73 % in the WB region; Figure 4a), in the form of the work of eddy-total flow interactions (53 % in the WB region; Figure 4d). EPW represents EKE transport done by the linear part of variability, usually interpreted as the wave dynamics. Its cumulated contribution in the WB region is dominated by the EKE export along the southern current branch ($EPW > 0$), where mesoscale variability is high. EPW is dominated by the coupled geostrophic-ageostrophic EKE flux. A scaling analysis (Eq. 16) shows that for typical mesoscale eddies dynamics in the WB region, the partially ageostrophic EPW dominates the geostrophic EPW due to the β-effect.

The geostrophic approximation is required by the use of η and is the most critical approximation to infer the EKE flux divergence. In the WB region, the approximation is valid for the $AEKE$ component, which dominates the EKE flux divergence. The use of η to infer the EKE flux divergence therefore leads to a fairly good qualitative degree of accuracy, even if it significantly underestimates its magnitude in the WB region (46 %).

Approximations (ii) (η primarily reflecting the 1^{st} baroclinic mode) and (iii) (weak topographic interactions) are less critical, but significantly bias the interpretation and accuracy of the EKE flux divergence. Both approximations are not directly required by the use of η field and can potentially be relaxed using other datasets in addition to satellite altimetry data. Numerical outputs and bathymetry data would respectively be needed to derive η partitioning between vertical modes (approximation (ii)) and the contribution of the EKE flux-topographic interactions (approximation (iii)).

7 Summary and Discussion

7.1 Summary

We have assessed the mesoscale EKE flux divergence in the region of the Agulhas Current as well as the use of sea surface height (η) to infer it, using a numerical simulation. The η-based EKE flux divergence is a reliable qualitative estimate of the true one (54 %), via one of its component – the advection of EKE by the total flow ($AEKE$; Figure 4). It is in favor of the use of satellite altimetry data to infer the net mesoscale EKE sources and sinks in the region of the Agulhas Current.

7.2 Discussion

Our study supports the WB region of the Agulhas Current as a hotspot of mesoscale eddy generation, whose energy is then exported (EKE flux divergence > 0; Figures 2b and 4b). It is in contrast with the paradigm of the decay of remotely-generated mesoscale

eddies at western boundaries (EKE flux divergence < 0), likely due to direct EKE routes channeled by topography (Zhai et al., 2010; Chelton et al., 2011; Evans et al., 2020; Z. Yang et al., 2021; Evans et al., 2022).

The latter paradigm relies on the β-effect being the main contribution to the EKE flux divergence (Zhai et al., 2010). Our analysis shows that this contribution is weak for the mesoscale regime in the WB region, explaining the different paradigms. The weak β-contribution is assessed using a scale analysis. In the WB region, the typical scale of mesoscale eddies falls in the range of a partially ageostrophic-dominated EPW, compared to the purely geostrophic EPW, which reduces to the β-contribution (Eq. 13; Figure 3b dn Appendix C). In the WB region, purely geostrophic flows – others than the β-effect – contribute significantly to the EKE flux divergence, via $AEKE$ (nonlinear component). The scale analysis shows the sensitivity of the EKE flux divergence to metrics set by the regional mesoscale dynamics. It can vary within western boundary regions across latitudes and across oceanic gyres, possibly pointing toward opposite contributions to the EKE flux divergence. The paradigm of the decay of remotely-generated mesoscale eddies may therefore be valid in specific oceanic regions.

The leading order processes of the mesoscale EKE budget in western boundary regions allow to further interpret the mesoscale EKE flux divergence. In the Agulhas Current, a study showed that the mainly positive mesoscale EKE flux divergence results from the local generation of EKE by instability processes of the current, overcoming the local EKE decay by topographically-channeled interactions and dissipation due to bottom-friction and wind (Tedesco et al., 2022). It is in contrast with studies at a mid-latitude western boundary, free of a western boundary current, which showed that the decay of remotely-generated mesoscale eddies is due to a zoo of topographically-channeled processes triggering direct EKE routes to dissipation (Evans et al., 2020, 2022). In the same way, a study simulating an idealized western boundary, free of a mean current, showed a mesoscale eddies decay due to topographically-channeled turbulence in the presence of rough topography (Z. Yang et al., 2021). The different studies suggest that in the presence of an intense mean current, the local generation of EKE may overcome the local decay, while in the absence of intense generation processes, the local EKE decay will likely dominate.

In a nutshell, the different studies suggest that, western boundary regions would be the place of contrasted mesoscale EKE flux divergence depending on regional factors. However, the validity of our discussion in the context of other WB regions is to consider cautiously, as the different studies are based in different western boundary regions and use different methods. It would require additional studies of other western boundary regions, including or excluding a mean current, to conclude on the western boundary regions dynamics and their contributions to the global ocean energy budget. Some elements of response on mesoscale eddy dynamics generic to western boundaries can be found using numerical simulations (Qiu et al., 2018; Torres et al., 2018). The SWOT mission presents the potential to test at a global scale the suggestion that western boundaries have contrasted contributions to the global ocean energy budget.

Appendix A Sensitivity of the true EPW to spatial smoothing

The true EPW (Eq. 4) is spatially smoothed to emphasize the large-scale patterns driving its cumulative contribution in the WB region.
The unsmoothed EPW term is characterized by small-scales patterns that are the most intense at topographic features – shelf slope (1000 m isobath), seamounts, canyons, roughness, etc – locally peaking at $O(2.5 - 10)$ W m^{-2} (Figure A1a). The intense small-scales patterns are larger by an order of magnitude than the unsmoothed $EPW_{(i,ii,iii)}$ term in the WB region ($O(0.001\text{-}0.1)$ W m^{-2}; Figure 2a). However, EPW has a cumulative contribution in the WB region (1.31 GW; Figure A1a) close to the one of $EPW_{(i,ii,iii)}$ (-1.33 GW; Figure 2a), regardless of the intense small-scale patterns. It indicates that the intense small-scale patterns locally compensate and do not significantly contribute to the EPW cumulative contribution in the WB region.

The sensitivity of the true EPW (Eq. 4) to the smoothing is shown using a Gaussian kernel of progressively increasing length scale : from 35 km, the spatially-averaged Rd over the dx $\sim$ 2.5 km grid, to 50 km and to 75 km, two typical mesoscale eddies radii at mid-latitudes as inferred from satellite altimetry (Chelton et al., 2011) (Figure A1). While the patterns of EPW significantly change with the different smoothing length scales, the order of magnitude of the cumulative contribution in the WB is fairly unchanged.
In the Figures of the present study, the label 'smoothed' refers to the Gaussian kernel using a 75 km-radius. Both smoothings, using a 50 km- or a 75 km-radius, result in fairly close cumulative EPW contributions in the WB region (Figures A1c,d). The 75 km-radius smoothing provides smoother patterns, emphasizing the most the large-scale patterns driving the EPW cumulative contribution in the WB region and easing the most its comparison with $EPW_{(i,ii,iii)}$ (Eq. 10).

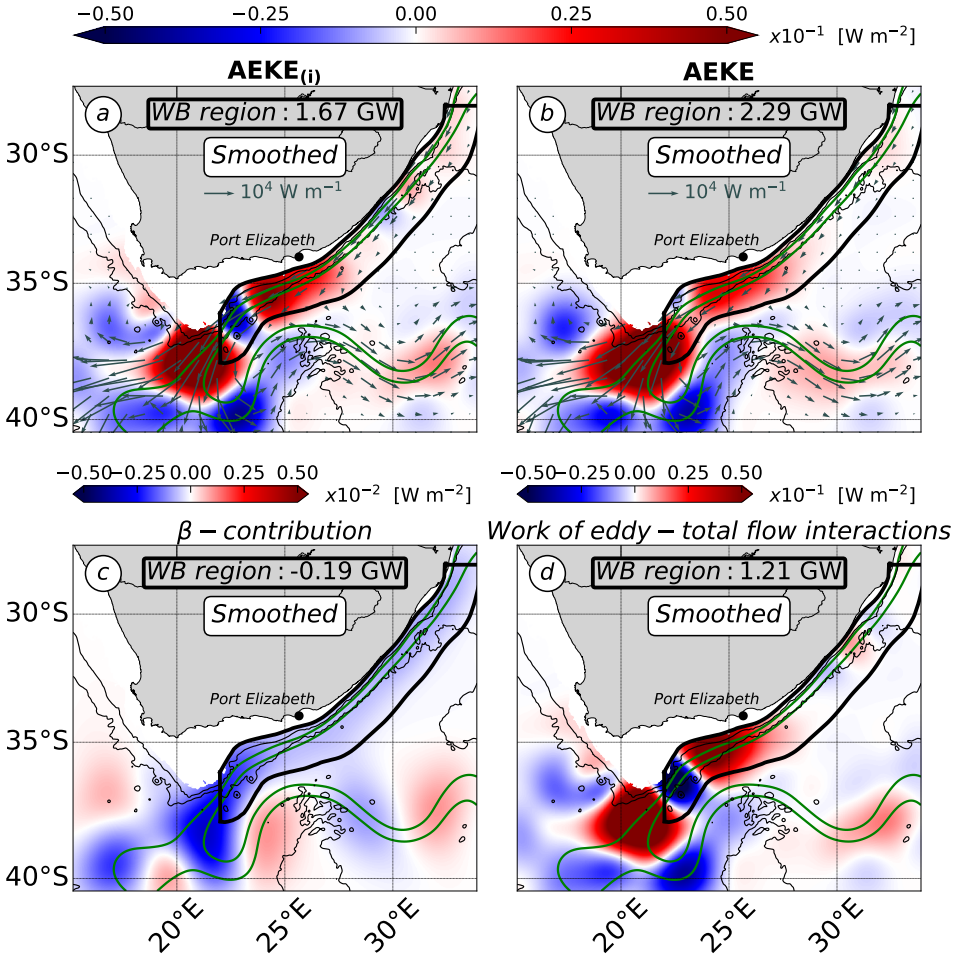

Figure 4: (a) $AEKE_{(i)}$ (Eq. 8), (b) $AEKE$ (Eq. 6), (c) β-contribution (**A**) to $AEKE_{(i)}$ and (d) contribution of work of the eddy-total flows interactions (**B**) to $AEKE_{(i)}$ [W m^{-2}]. Terms are smoothed using a 75 km-radius Gaussian kernel. Note the magnitude difference between (a,b,d) and (c). (a,b) Vector fields denote the EKE flux ($\frac{\rho_0}{2}\int_{-H}^{\eta}\mathbf{u}\phi_n||\mathbf{u}'_n\phi_n||^2\,dz$ with $n=0-1$) using (a) geostrophic ($\mathbf{u}_{n,g}\phi_n = \mathbf{k}\wedge\frac{g}{f}\nabla_H\left(\frac{\phi_n}{|\phi_n|}\lambda_n\eta\right)$ with $\lambda_n = \frac{\eta_n}{\eta}$) and (b) total velocity fields ($\mathbf{u}_n\phi_n$) [W m^{-1}]. (cf. Figure 1 for a detailed caption). (a) $AEKE_{(i)}$ is dominated by (d) the work of eddy-total flows interactions and is a reliable estimate of (b) the true mesoscale $AEKE$.

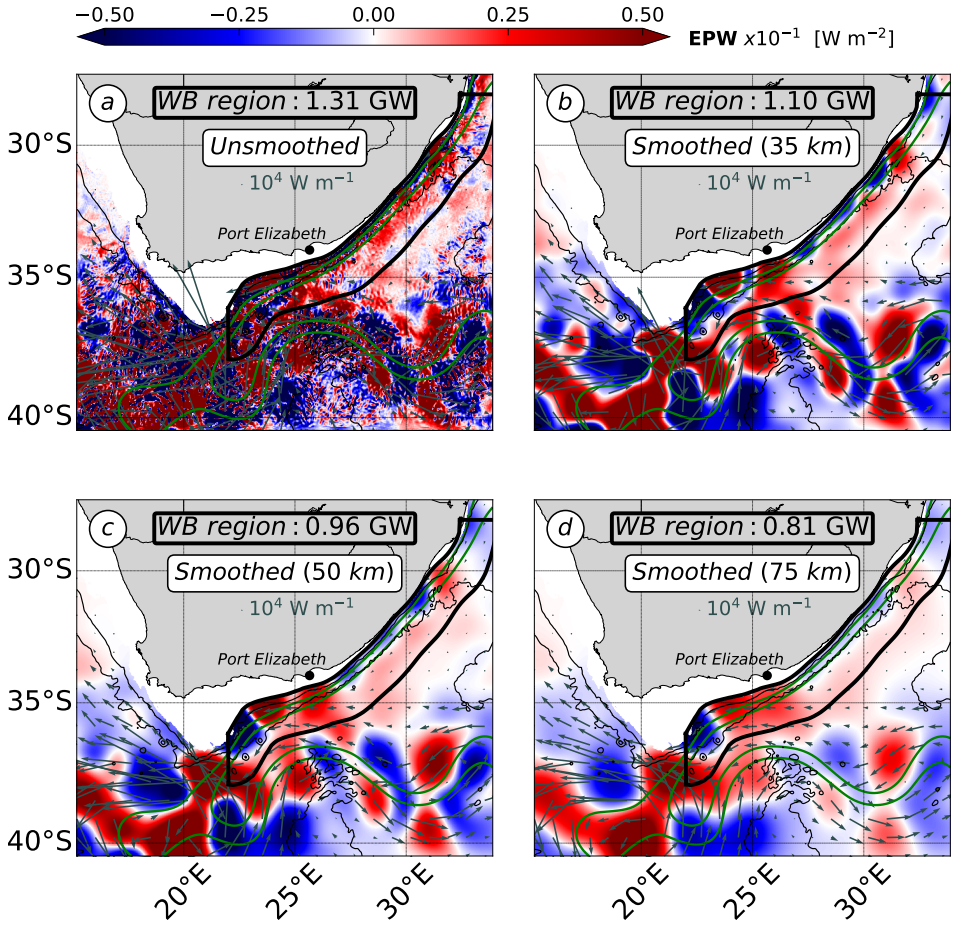

Figure A1: (a) Unsmoothed and (b,c,d) smoothed true mesoscale EPW terms (Eq. 5) [W m^{-2}]. The radius of the Gaussian kernel used for smoothing varies from (b) 35 km, (c) 50 km to (d) 75 km. Vector fields denote the EKE flux ($\int_{-H}^{\eta} \mathbf{u}'_n p'_n \phi_n^2 \, dz$ with $n = 0 - 1$) [W m^{-1}]. (cf. Figure 1 for a detailed caption). (d) The 75 km-radius smoothing length scale, a typical radius of mesoscale eddy at mid-latitudes (Chelton et al., 2011), emphasizes the large-scale patterns driving the cumulative contribution of the true EPW in the WB region and eases its comparison with $EPW_{(i,ii,iii)}$ (Eq. 10; Figure 1c).

Appendix B Partitioning of η variance between the barotropic and 9 first baroclinic modes

The partitioning of the η variance (η'^2) between the vertical modes (α_n^2) is used to define $EPW_{(i,iii)}$ (Eq. 11), an adjusted expression of $EPW_{(i,ii,iii)}$ (Eq. 10), in order to evaluate approximation (ii) of η field primarily reflecting the 1^{st} baroclinic mode (section 2.1.3.2).

We limit our analysis to the barotropic and 9 first baroclinic modes which capture 85-100 % of the modeled η'^2 in the Agulhas Current region (not shown). η is a 2D field and cannot be projected on the vertical mode base ϕ_n, but the η modal coefficient (η_n) is inferred using the relation $|p|_{z=0} = \rho_0 g \eta$, as follows : $\eta_n = \frac{1}{\rho_0 g} \frac{p_n}{|\phi_n|_{z=0}}$. The modal expression of η'^2 is derived and α_n^2 defined as follows :

$$\eta'^2 = \sum_{n=0}^{\infty} \eta'_n \sum_{m=0}^{\infty} \eta'_m = \sum_{n=0}^{\infty} \eta_n'^2 + \underbrace{\sum_{n=0}^{\infty} \sum_{m \neq n}^{\infty} \eta'_n \eta'_m}_{Intermodal\ coupling\ (C_{nm})} = \sum_{n=0}^{\infty} \eta_n'^2 + C_{nm} \tag{B1}$$

$$\alpha_n^2 = \frac{\eta_n'^2}{\eta'^2} \ ; \ \alpha_{nm} = \frac{C_{nm}}{\eta'^2} \tag{B2}$$

The modal expression of η'^2 involves an intermodal coupling term C_{nm} (B1). It corresponds to a phase-locked combination of vertical modes due to the modal correlation in time at the surface (Wunsch, 1997; Scott & Furnival, 2012). The degree of the modeled modal correlation at the surface ($\frac{\sum_{n=0}^{9} \eta_n'^2}{\sum_{n=0}^{9} \eta_n'^2 + C_{nm}}$) is 1.8 in average in the Agulhas Current region, which is consistent with the 2-3 factor determined from *in situ* data at global-scale by Wunsch (1997). It must be noted that the true EPW (Eq. 5) implies the orthogonality condition (resulting in canceling out the C_{nm} term) and that it therefore only accounts for the contributions of the individual vertical modes categories ($n = 0$ and $n = 1$).

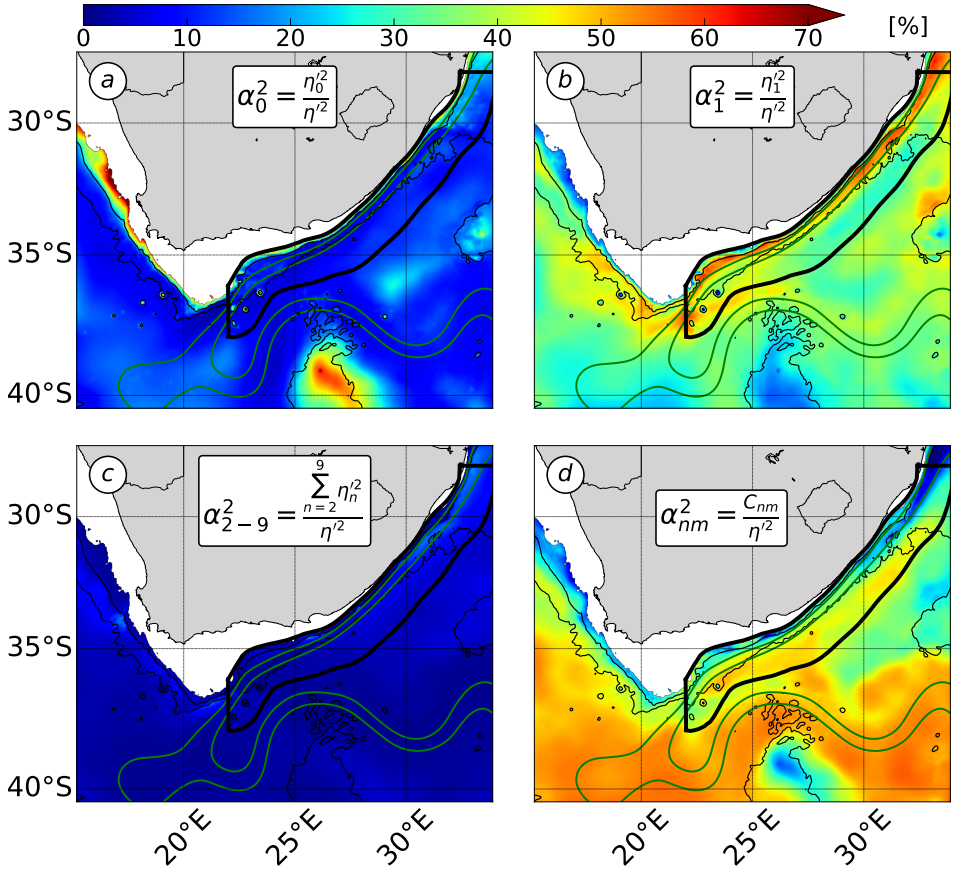

Figure B1: Partitioning of η variance (α_n^2) between the vertical modes categories : (a) $n = 0$, (b) $n = 1$, (c) $n = 2-9$ and (d) the intermodal coupling term C_{nm} [%] (Eq. B1). (cf. Figure 1 for a detailed caption). The η variance largely partitions into (b) the 1^{st} baroclinic mode and more weakly into (a) the barotropic mode, which both contribute to $EPW_{(i,iii)}$ (Eq. 11; Figure 2c).

η'^2 mainly partitions into the individual 1^{st} baroclinic mode (38 $\pm$ 2 % in the WB region) and the intermodal coupling term (36 $\pm$ 2 % in the WB region). It also partitions more weakly, but still significantly into the individual barotropic mode (16 $\pm$ 4 % in the WB region) (Figure B1). The partitioning of η'^2 is partially consistent with the usual interpretation of η primarily reflecting the 1^{st} baroclinic mode (Wunsch, 1997; Smith & Vallis, 2001). However, it indicates that the vertical structure of mesoscale eddies – formally represented by the combination of the barotropic ($n = 0$) and 1^{st} baroclinic modes ($n = 1$) (Wunsch, 2007; Smith & Vallis, 2001; Venaille et al., 2011; Tedesco et al., 2022) – can be accurately inferred from η field.

Appendix C Contribution of ageostrophic motions to the true *EPW* by the Rhines scale

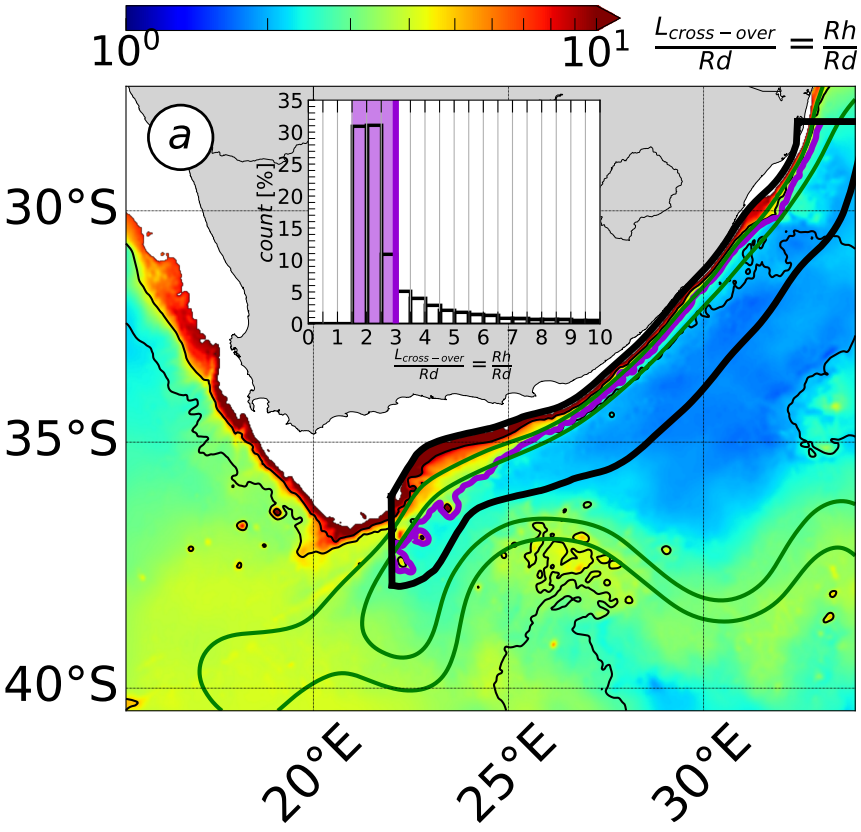

Figure C1: (a) Ratio $\frac{L_{cross-over}}{Rd} = \frac{Rh}{Rd}$ ($Rh = \frac{1}{H}\int_{-H}^{\eta}\left(\sqrt{\frac{||\mathbf{u}'||}{\beta}}\right) dz$, with $||\mathbf{u}'||$ the magnitude of mesoscale eddies velocity). The purple line denotes $\frac{Rh}{Rd}$ 70 % percentile, the green contours denote the 0.25 m and 0.5 m isolines of time-averaged η and black contours denote the 1000 m and 3000 m isobaths. The terms count in the WB region [%] is shown as barplot, where purple shaded areas denote the 70 % percentile range of values. (a) $\frac{Rh}{Rd} >> 1$ in the WB region, resulting in L_{eddy} ($\geq Rd$) to fall in the range of dominating partially ageostrophic EPW, compared to the β-effect.

The Rhines scale (Rh) is defined in turbulence geostrophic theory to mark the transition from an advectively-dominated ($Rh << L$) to a Rossby waves-dominated ($Rh >> L$) turbulent regime (Rhines, 1975). Rh is also emphasized by our scale analysis to mark the transition from a partially ageostrophic-dominated to a β-effect-dominated EPW (section 4.4).

We infer Rh for the mesoscale eddies simulated by the dx $\sim$ 2.5 km numerical grid, as follows : $Rh = \frac{1}{H}\int_{-H}^{\eta}\left(\sqrt{\frac{||\mathbf{u}'||}{\beta}}\right)\,dz$ with $||\mathbf{u}'||$ the magnitude of mesoscale eddies velocity. $\frac{Rh}{Rd} \sim O(1.5-3)Rd$ in 70 % of the WB region, with larger ratio located at the inner front of the Agulhas Current (Figure C1). It results in L_{eddy} ($L_{eddy} \geq Rd$) to fall in the WB region in the range of an advectively-dominated turbulent.

Along with $L_{cross-over} = \frac{\zeta'_{RMS}}{\beta}$ (Eq. 13; Figure 3b), Rh confirms that the partially ageostrophic EPW dominates the β-effect. It questions the use of satellite altimetry data to infer EPW (Eq. 4). However, the impact of the geostrophic approximation (i) on $AEKE$ must be assessed to conclude on the use of satellite altimetry data to infer the EKE flux divergence.

Acknowledgments

This work was granted access to the HPC resources of IDRIS under the allocation A0040107630 made by GENCI at Paris, France, and of the HPC facilities DATARMOR of "Pôle de Calcul Intensif pour la Mer" at Ifremer, Brest, France. This work was supported by the Ifremer and the Brittany region for PhD funding. We also gratefully acknowledge support from the French National Agency for Research (ANR) through the projects DEEPER (ANR-19-CE01-0002-01) and the project DIEGO of the CNES/TOSCA SWOT program. WOES36 model outputs are available online at `http://dap.saeon.ac.za/thredds/catalog/SAEON.EGAGASINI/2019.Penven/DAILY_MEANS/1_36_degree/catalog.html` (DOI: 10.15493/SAEON.EGAGASINI.10000 The AVISO data are available at `www.aviso.altimetry.fr`, the WOA18 and WOCE climatologies are available at `www.nodc.noaa.gov/OC5/woa18/` and `https://icdc.cen.uni-hamburg.de/thredds/catalog/ftpthredds/woce/catalog.htm`.

References

Adcock, S., & Marshall, D. (2000). Interactions between geostrophic eddies and the mean circulation over large-scale bottom topography. *Journal of physical oceanography*, *30*(12), 3223–3238.

Capó, E., Orfila, A., Mason, E., & Ruiz, S. (2019). Energy conversion routes in the western mediterranean sea estimated from eddy–mean flow interactions. *Journal of Physical Oceanography*, *49*(1), 247–267.

Charney, J. G. (1971). Geostrophic turbulence. *Journal of the Atmospheric Sciences*, *28*(6), 1087–1095.

Chelton, D., Deszoeke, R., Schlax, M., El Naggar, K., & Siwertz, N. (1998). Geographical variability of the first baroclinic Rossby radius of deformation. *Journal of Physical Oceanography*, *28*(3), 433–460.

Chelton, D., Schlax, M., & Samelson, R. (2011). Global observations of nonlinear mesoscale eddies. *Progress in oceanography*, *91*(2), 167–216.

Chelton, D., Schlax, M., Samelson, R., & de Szoeke, R. (2007). Global observations of large oceanic eddies. *Geophysical Research Letters*, *34*(15).

Chen, R., Flierl, G., & Wunsch, C. (2014). A description of local and nonlocal eddy–mean flow interaction in a global eddy-permitting state estimate. *Journal of Physical Oceanography*, *44*(9), 2336–2352.

Cushman-Roisin, B., & Beckers, J.-M. (2011). *Introduction to geophysical fluid dynamics: physical and numerical aspects*. Academic press.

Debreu, L., Marchesiello, P., Penven, P., & Chambon, G. (2012). Two-way nesting in split-explicit ocean models: Algorithms, implementation and validation. *Ocean Modelling*, *49-50*, 1-21.

Ducet, N., Traon, P.-Y. L., & Reverdin, G. (2000). Global high-resolution mapping of ocean circulation from TOPEX/Poseidon and ERS-1 and-2. *Journal of Geophysical Research: Oceans*, *105*(C8), 19477–19498.

Elipot, S., & Beal, L. M. (2015). Characteristics, Energetics, and Origins of Agulhas Current Meanders and Their Limited Influence on Ring Shedding. *Journal of Physical Oceanography*, *45*(9), 2294-2314. doi: 10.1175/JPO-D-14-0254.1

Evans, D., Frajka-Williams, E., & Garabato, A. N. (2022). Dissipation of mesoscale eddies at a western boundary via a direct energy cascade. *Scientific Reports*, *12*(1), 1–13.

Evans, D., Frajka-Williams, E., Garabato, A. N., Polzin, K., & Forryan, A. (2020). Mesoscale eddy dissipation by a 'zoo' of submesoscale processes at a western boundary. *Journal of Geophysical Research: Oceans*, e2020JC016246.

Ferrari, R., & Wunsch, C. (2009). Ocean circulation kinetic energy: Reservoirs, sources, and sinks. *Annual Review of Fluid Mechanics*, *41*.

Gill, A. (1982). *Atmosphere-ocean dynamics (international geophysics series)*. academic press.

Gill, A., Green, J., & Simmons, A. (1974). Energy partition in the large-scale ocean circulation and the production of mid-ocean eddies. *Deep sea research and oceanographic abstracts*, *21*(7), 499–528.

Gouretski, V., & Koltermann, K. (2004). WOCE global hydrographic climatology. *Berichte des BSH*, *35*, 1–52.

Gula, J., Molemaker, M., & McWilliams, J. (2015). Gulf Stream dynamics along the Southeastern U.S. Seaboard. *J. Phys. Oceanogr.*, *45*(3), 690-715.

Gula, J., Molemaker, M., & McWilliams, J. (2016). Submesoscale dynamics of a Gulf Stream frontal eddy in the South Atlantic Bight. *Journal of Physical Oceanography*, *46*(1), 305–325.

Halo, I., Penven, P., Backeberg, B., Ansorge, I., Shillington, F., & Roman, R. (2014). Mesoscale eddy variability in the southern extension of the East Madagascar Current: Seasonal cycle, energy conversion terms, and eddy mean properties. *Journal of Geophysical Research: Oceans*, *119*(10), 7324–7356.

Harrison, D. E., & Robinson, A. R. (1978). Energy analysis of open regions of turbulent flows—Mean eddy energetics of a numerical ocean circulation experiment. *Dynamics of Atmospheres and Oceans*, *2*(2), 185–211.

Jamet, Q., Deremble, B., Wienders, N., Uchida, T., & Dewar, W. (2021). On wind-driven energetics of subtropical gyres. *Journal of Advances in Modeling Earth Systems*, *13*(4), e2020MS002329.

Kang, D., & Curchitser, E. (2015). Energetics of eddy–mean flow interactions in the Gulf Stream region. *Journal of Physical Oceanography*, *45*(4), 1103–1120.

Kelly, S. (2016). The vertical mode decomposition of surface and internal tides in the presence of a free surface and arbitrary topography. *Journal of Physical Oceanography*, *46*(12), 3777–3788.

Kelly, S., Nash, J., & Kunze, E. (2010). Internal-tide energy over topography. *Journal of Geophysical Research: Oceans*, *115*(C6).

Kelly, S., Nash, J., Martini, K., Alford, H. M., & Kunze, E. (2012). The cascade of tidal energy from low to high modes on a continental slope. *Journal of physical oceanography*, *42*(7), 1217–1232.

Li, J., Roughan, M., & Kerry, C. (2021). Dynamics of interannual eddy kinetic energy modulations in a western boundary current. *Geophysical Research Letters*, e2021GL094115.

Locarnini, M., Mishonov, A., Baranova, O., Boyer, T., Zweng, M., Garcia, H., ... others (2018). *World ocean atlas 2018, volume 1: Temperature* [Dataset]. ARCHIMER. Retrieved from `https://data.nodc.noaa.gov/woa/WOA18/DOC/woa18_vol1.pdf`

Lutjeharms, J. (2006). *The Agulhas Current* (Vol. 2). Springer.

Masuda, A. (1978). Group velocity and energy transport by Rossby waves. *Journal of Oceanography*, *34*(1), 1–7.

Müller, P., McWilliams, J., & Molemaker, M. (2005). *Routes to dissipation in the ocean: The 2D/3D turbulence conundrum.* Cambridge University Press Cambridge.

Nikurashin, M., & Ferrari, R. (2010). Radiation and dissipation of internal waves generated by geostrophic motions impinging on small-scale topography: Theory. *Journal of Physical Oceanography*, *40*(5), 1055–1074.

Paldor, N., & Lutjeharms, J. (2009). Why is the stability of the Agulhas Current geographically bi-modal? *Geophysical Research Letters*, *36*(14), n/a–n/a. Retrieved from `http://dx.doi.org/10.1029/2009GL038445` (L14604) doi: 10.1029/2009GL038445

Perfect, B., Kumar, N., & Riley, J. (2020). Energetics of Seamount Wakes. Part I: Energy Exchange. *Journal of Physical Oceanography*, *50*(5), 1365–1382.

Qiu, B., Chen, S., Klein, P., Wang, J., Torres, H., Fu, L.-L., & Menemenlis, D. (2018). Seasonality in transition scale from balanced to unbalanced motions in the world ocean. *Journal of Physical Oceanography*, *48*(3), 591–605.

Rhines, P. (1975). Waves and turbulence on a beta-plane. *Journal of Fluid Mechanics*, *69*(3), 417–443.

Scott, R., & Furnival, D. (2012). Assessment of traditional and new eigenfunction bases applied to extrapolation of surface geostrophic current time series to below the surface in an idealized primitive equation simulation. *Journal of physical oceanography*, *42*(1), 165–178.

Shchepetkin, A., & McWilliams, J. (2005). The Regional Oceanic Modeling System (ROMS): A split-explicit, free-surface, topography-following- coordinate ocean model. *Ocean Modelling*, *9*, 347-404.

Smith, K., & Vallis, G. (2001). The scales and equilibration of midocean eddies: Freely evolving flow. *Journal of Physical Oceanography*, *31*(2), 554–571.

Tedesco, P., Gula, J., Ménesguen, C., Penven, P., & Krug, M. (2019). Generation of submesoscale frontal eddies in the Agulhas Current. *Journal of Geophysical Research: Oceans*, *124*(11), 7606–7625.

Tedesco, P., Gula, J., Penven, P., & Ménesguen, C. (2022). Mesoscale Eddy Kinetic Energy budgets and transfers between vertical modes in the Agulhas Current. *Journal of Physical Oceanography*.

Torres, H., Klein, P., Menemenlis, D., Qiu, B., Su, Z., Wang, J., ... Fu, L.-L. (2018). Partitioning ocean motions into balanced motions and internal gravity waves: A modeling study in anticipation of future space missions. *Journal of Geophysical Research: Oceans*, *123*(11), 8084–8105.

Venaille, A., Vallis, G., & Smith, K. (2011). Baroclinic turbulence in the ocean: Analysis with primitive equation and quasigeostrophic simulations. *Journal of Physical Oceanography*, *41*(9), 1605–1623.

Vic, C., Roullet, G., Carton, X., & Capet, X. (2014). Mesoscale dynamics in the Arabian Sea and a focus on the Great Whirl life cycle: A numerical investigation using ROMS. *Journal of Geophysical Research: Oceans*, *119*(9), 6422–6443.

Wunsch, C. (1997). The vertical partition of oceanic horizontal kinetic energy. *Journal of Physical Oceanography*, *27*(8), 1770–1794.

Wunsch, C. (2007). The past and future ocean circulation from a contemporary perspective. *Geophysical Monograph-American Geophysical Union*, *173*, 53.

Yan, X., Kang, D., Curchitser, E., & Pang, C. (2019). Energetics of eddy–mean flow interactions along the western boundary currents in the North Pacific. *Journal of Physical Oceanography*, *49*(3), 789–810.

Yang, Y., & Liang, X. S. (2016). The instabilities and multiscale energetics underlying the mean–interannual–eddy interactions in the Kuroshio Extension region. *Journal of Physical Oceanography*, *46*(5), 1477–1494.

Yang, Z., Zhai, X., Marshall, D., & Wang, G. (2021). An Idealized Model Study of Eddy Energetics in the Western Boundary "Graveyard". *Journal of Physical Oceanography*, *51*(4), 1265–1282.

Yankovsky, E., Zanna, L., & Smith, K. (2022). Influences of Mesoscale Ocean Eddies on Flow Vertical Structure in a Resolution-Based Model Hierarchy. *Earth and Space Science Open Archive*, 60. Retrieved from `https://doi.org/10.1002/essoar.10511501.1` doi: 10.1002/essoar.10511501.1

Zhai, X., Johnson, H., & Marshall, D. (2010). Significant sink of ocean-eddy energy near western boundaries. *Nature Geoscience*, *3*(9), 608.

Zweng, M., Seidov, D., Boyer, T., Locarnini, M., Garcia, H., Mishonov, A., ... others (2019). *World ocean atlas 2018, volume 2: Salinity* [Dataset]. ARCHIMER. Retrieved from `https://data.nodc.noaa.gov/woa/WOA18/DOC/woa18_vol2.pdf`